

ROS 2-based Implementation of Advanced Control for a Teleoperated Surgical Robot

Master Thesis

In partial fulfillment of the requirements for the degree

"Master of Science in Engineering"

Study program:

**Mechatronics and Smart Technologies - Mechanical
Engineering**

Management Center Innsbruck

Supervisor:

FH-Prof. Yeongmi Kim, PhD

Author:

Liam Joseph Nolan

52315010

Declaration in Lieu of Oath

„I hereby declare, under oath, that this master thesis has been my independent work and has not been aided with any prohibited means. I declare, to the best of my knowledge and belief, that all passages taken from published and unpublished sources or documents have been reproduced whether as original, slightly changed or in thought, have been mentioned as such at the corresponding places of the thesis, by citation, where the extend of the original quotes is indicated.“

Place, Date

Signature

Acknowledgement

First and foremost, I would like to thank my supervisor, Prof. Yeongmi Kim, PhD. This research would not have been possible without her tireless dedication, support, and willingness to sacrifice sleep and good weather in the pursuit of robotic excellence. I would also like to thank my colleague, Michael Messner, for his support in repairing the system no matter how many times I managed to break it in new and exciting ways. I would also like to thank Darren Collins both for being the catalyst of my career in robotics and for inspiring countless other roboticists through his work with FRC team 2046. Finally, I would like to thank my father, Joseph Nolan, for not only providing me the brain necessary to conduct this research, but also for his constant support throughout the years.

Abstract

The advancement of laparoscopic surgical robotics has contributed significant progress to the field of minimally invasive surgery; however, their high cost limits widespread adoption in research and training efforts. This system utilizes affordable, off-the-shelf hardware to produce an accessible development platform for research purposes. The system utilizes ROS 2's distributed framework in an effort to improve real-time system performance and enable future software architecture scalability. Advanced system identification methods were employed to characterize the system, and an advanced control strategy was designed around this characterization. Experimental validation has demonstrated the system's ROS 2 based architecture in combination with the advanced system identification and control methods reduced system positional error by up to 92.1% over the previous implementation while also offering improved system scalability. The results found through these experimental tests confirm the feasibility of a cost-effective surgical robotic system with advanced control strategies, contributing to the advancement and accessibility of the next generation of robotic assisted surgical systems.

Keywords: Advanced Control Engineering, LQR Control, LQI Control, Feedforward Control, ROS 2, Nonlinear Control, Gain Scheduling, Medical Robotics, Laparoscopic Surgery

Contents

1. Introduction	1
1.1. Background and Context	1
1.2. Problem Statement	1
1.3. Research Aim and Objectives	2
1.4. Scope	2
2. Background and State of the Art	4
2.1. The da Vinci Research Kit	4
2.2. The Raven II Surgical System	5
2.3. Robot Operating System 2	6
2.4. Control Techniques in Robotic Surgery	7
2.5. System Identification Techniques in Robotic Surgery	8
2.6. Summary and Research Motivation	8
3. Desktop Teleoperated Surgical Training System	9
3.1. Overall System Architecture	9
3.1.1. MTM Overview	10
3.1.2. PSM Overview	11
3.2. MTM Mechanical Design	12
3.2.1. Superstructure Design	13
3.2.2. Arm Joint Design	13
3.3. MTM Electrical Architecture	15
3.3.1. System Overview	15
3.3.2. Joint Subsystems	15
3.3.3. Gimbal Subsystem	16
3.4. PSM Mechanical Design	16
3.4.1. Overview	16
3.4.2. Superstructure	16
3.4.3. Roll Axis	17

3.4.4. Pitch Axis	18
3.4.5. Insertion Axis	19
3.4.6. Tool Cart and End Effector	20
3.5. PSM Electrical Architecture	21
3.6. System Software Architecture	22
3.6.1. MTM Software	22
3.6.2. PSM Software	22
3.7. System Controller Design	23
3.8. System Kinematics and Coordinate Frames	23
3.8.1. MTM Coordinate Frame	23
3.8.2. PSM and Tool Coordinate Frame	25
4. Implementation on Current Hardware	26
4.1. Software Architecture	26
4.1.1. ROS 2 System Architecture	26
4.1.2. MTM Modeling and Visualization	27
4.1.3. MicroROS Implementation	28
4.1.4. MTM Data Streaming and filtering	30
4.1.5. MTM to PSM Communication Protocol	30
4.1.6. PSM Software	32
4.2. System Identification	35
4.2.1. Roll Joint Open Loop Step Response	35
4.2.2. Closed Loop Excitation Through PRBS	36
4.2.3. Multi-point System Identification	37
4.3. Controller Design	42
4.3.1. Original PID Controller	42
4.3.2. MPC	43
4.3.3. Gain Scheduling and Adaptive Control	43
4.3.4. LQR and LQI Control	46
4.3.5. Feedforward Control	51
4.3.6. Comprehensive Control Strategy	52
5. System evaluation	53
5.1. Overview of Experiments	53
5.2. Control Algorithm Performance	54
5.2.1. Sinusoidal Path Following Experiment Results	54

5.2.2. Target Following Experiment	58
6. Conclusion and Future Work	61
6.1. Key Findings	61
6.2. Limitations	61
6.3. Recommendations for Future Work	62
6.4. Final Remarks	62
Bibliography	VIII
List of Figures	X
List of Tables	XI
A. Source Code Repositories	XII
A.1. PSM Firmware	XII
A.2. MTM Firmware	XII
A.3. MATLAB Scripts	XII
A.4. MTM SDF Model	XII
A.5. MTM Joint Publisher	XIII

1. Introduction

1.1. Background and Context

Laparoscopic surgery offers a minimally invasive option, significantly cutting down on patients' postoperative pain and recovery time. Yet, the intricate dexterity this technique demands has created a clear need for robotic assistance. As a result of this need systems like Intuitive Surgical's da Vinci have been operating since 1999 [1]. While these systems have proven their ability at reducing recovery time, they also come with prohibitive costs and technical complexities, making them largely out of reach for many researchers. This creates barriers for further advancements in robotic assisted surgery and as a result, researchers at MCI previously developed an affordable, desktop operated surgical robotic system.

1.2. Problem Statement

While this system was originally effective in creating an affordable alternative to existing solutions, its dynamic performance and software architecture left significant room for improvements in performance. The software architecture was implemented using a C based Arduino framework. This lacked many features necessary for system development. Originally, the system was controlled with a tuned PID controller. This controller, while providing basic control over the system, lacked the performance necessary to carry out more complex and precise motion paths. The system was also highly nonlinear in nature, and as the control target deviated from the system origin point, its performance suffered, resulting in inadequate control behavior.

1.3. Research Aim and Objectives

The goal of the research conducted in this thesis was twofold. First, to implement a Robotic Operating System 2 (ROS 2) framework for the existing system. ROS 2 is the current industry standard open-source distributed robotics middleware framework, making it well suited for the dynamic, precision-focused requirements of surgical robotic systems. Its modular nature allows for the development of multiple complex subsystems in parallel, and its framework can be easily adapted to accommodate future additions or improvements to the platform. Additionally, ROS 2 offers many essential tools for complex robotic systems, such as system visualization, collision detection, and frame transformation frameworks. Porting the existing system to this ROS 2-based framework would allow access to these benefits and facilitate further development of the system in the future.

Secondly, due to the lack of dynamic performance and control in the current system, this research aimed to develop a more robust characterization and control strategy to address its nonlinear nature. The improved characterization strategy involves comparing the results of step response experiments to closed-loop excitation data to better model the system. More advanced control strategies, such as Linear Quadratic Regulator (LQR) and Linear Quadratic Integral (LQI) controllers with feedforward control, could then be applied to this system model. Additionally, gain scheduling techniques would be utilized to adapt the controller to the system's highly nonlinear behavior.

1.4. Scope

This thesis focuses on the implementation of an adaptive control framework within a ROS 2 based architecture for a teleoperative laparoscopic surgical robotic test platform. The scope of the research includes the migration of the existing robotic system from a C-based Arduino framework to ROS 2, the development of advanced control strategies to address system nonlinearities, and the experimental validation of the proposed control methods using a laboratory-scale test platform.

Clinical application and in vivo testing are beyond the scope of this work; thus, the system is evaluated exclusively in controlled lab environments. The research prioritizes software architecture and control performance over hardware design improvements. Furthermore, the adaptive control methods are tested on predefined motion trajectories

and system responses, which may not cover the full range of operational scenarios encountered in actual surgical procedures.

2. Background and State of the Art

This chapter serves as an overview of the current state of the art regarding low-cost teleoperative surgical training systems. This section will explore their architecture, advantages, and disadvantages. Additionally, this section will delve into current control standards and strategies that these systems use and will discuss the ROS 2 and its applications.

2.1. The da Vinci Research Kit

The da Vinci Research Kit (dVRK) is a research platform developed through a collaboration between academic institutions, Johns Hopkins University and Worcester Polytechnic Institute, and Intuitive Surgical Inc. in 2012. It consists of first-generation da Vinci components that allow for a common development platform between institutions for the research of robotic-assisted surgery. The dVRK consists of two da Vinci master tool manipulators (MTM), two da Vinci patient side manipulators (PSM), a stereo viewer, a foot pedal tray, manipulator interface boards (dMIBs), and a basic accessory kit. [2]

At the time of writing in 2025, the dVRK program has been used by 40 research centers in 10 countries [3]. It offers a high-performance platform for researchers using hardware that would otherwise be retired. However, it is not without its disadvantages. The system has a very large footprint; three different pieces of large capital equipment are required by this system, and it is not easily transportable. Additionally, the system is expensive to acquire and maintain, creating a high barrier to entry for many applications. Because of these limitations, researchers recognized the need for additional options in the surgical robotics research space. This ultimately resulted in the Raven II [4].

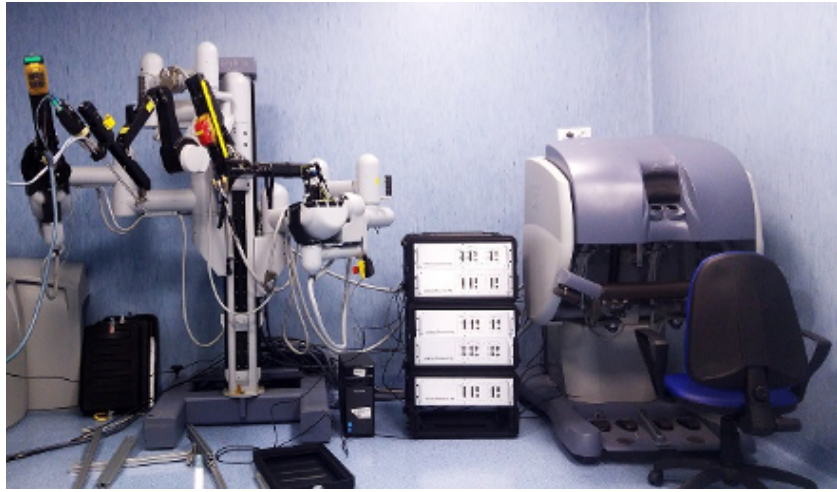


Figure 2.1.: The Original Da Vinci Research Kit.(Reprinted from [5] Fig 1)

2.2. The Raven II Surgical System

The **Raven II** is an open-architecture robotic surgical system developed by the University of Washington and the University of California, Santa Cruz. It is a low-cost alternative to the dVRK and draws much design inspiration from the original da Vinci's capstan cable drive system. The Raven II is a continuation of the original Raven system and was designed to be as modular as possible to make the system more portable than existing surgical systems. The Raven II system consists of two cable-driven PSMs, a cable-driven Mantis Duo MTM, a stereoscopic surgeon viewer, and control electronics.

Each of the Raven II's 7-DOF arms are remotely driven by a cable system powered by brushless DC motors. Encoders are directly coupled to the motors, which leads to difficulties in state estimation. Cable stretch and linkage flexure lead to discrepancies between the actual joint angles and the motor output. This design can be seen in **Figure 2.2.**

The Raven II is driven by the Mantis Duo. The MTM design features a novel approach where each MTM is suspended by four driven cables. These cables allow for simultaneous positional sensing of the surgeon's movements while providing haptic feedback.

While the Raven II is a smaller alternative to the dVRK, it still requires a significant investment in hardware, costing \$250,000 USD [7] for a complete system. This cost remains prohibitive for many research institutions and limits the system's accessibility.

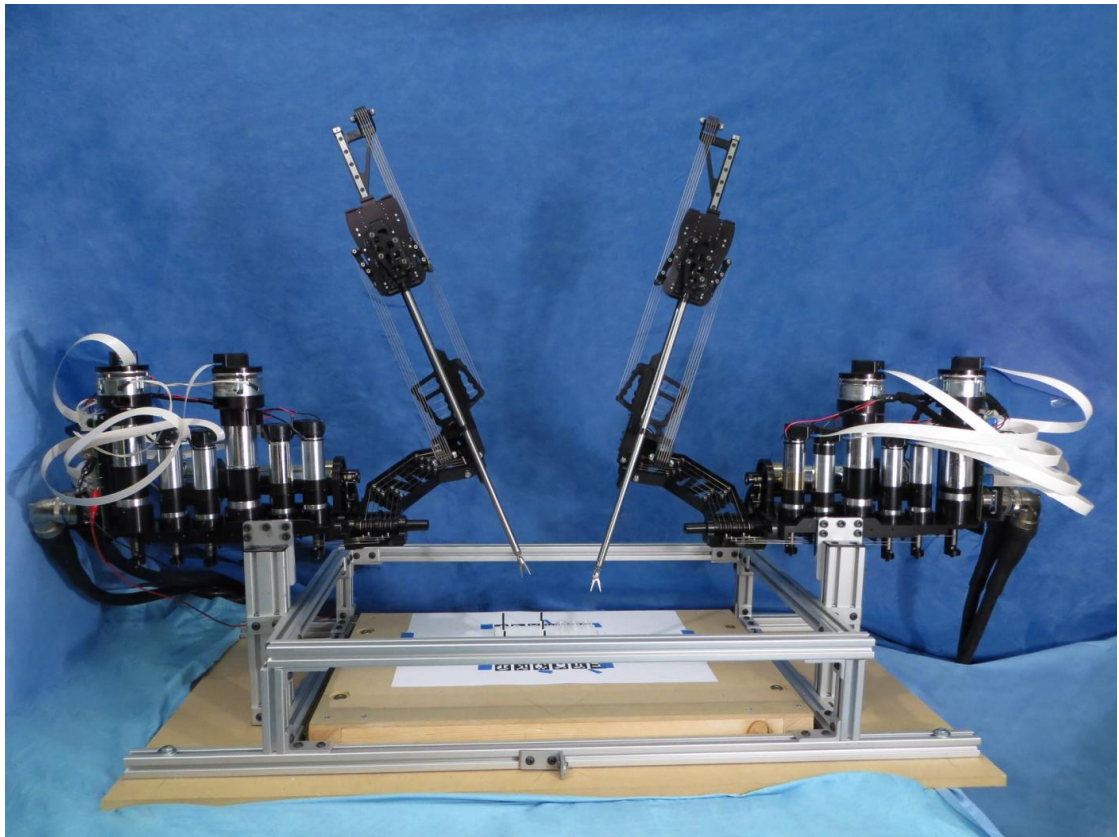


Figure 2.2.: The Raven II surgical system design. In this figure the cable driven design can clearly be seen (Reprinted from [6] Fig 1)

2.3. Robot Operating System 2

Robot Operating System 2 (ROS 2) is a Linux-based, open-source robotics middleware suite consisting of software frameworks for robotic applications. ROS 2 is a direct evolution of ROS 1 and improves upon many aspects. While ROS 1 relied on a centralized ROS Master, ROS 2 uses the Data Distribution Service (DDS) for decentralized, peer-to-peer communication, eliminating the single point of failure present in the master node and increasing system reliability. ROS 2 also provides full real-time performance and supports most common microcontrollers through Micro-ROS, which is critical for many modern applications.

ROS 2 has proven itself as an industry standard, being utilized frequently in cutting-edge applications such as autonomous vehicles, humanoid robotics, and even surgical robotics [8]. Its suite of tools and utilities provides researchers with valuable develop-

ment resources, including system visualization, collision detection, and frame transformation libraries, all of which are valuable assets to a Robotic Autonomous System.

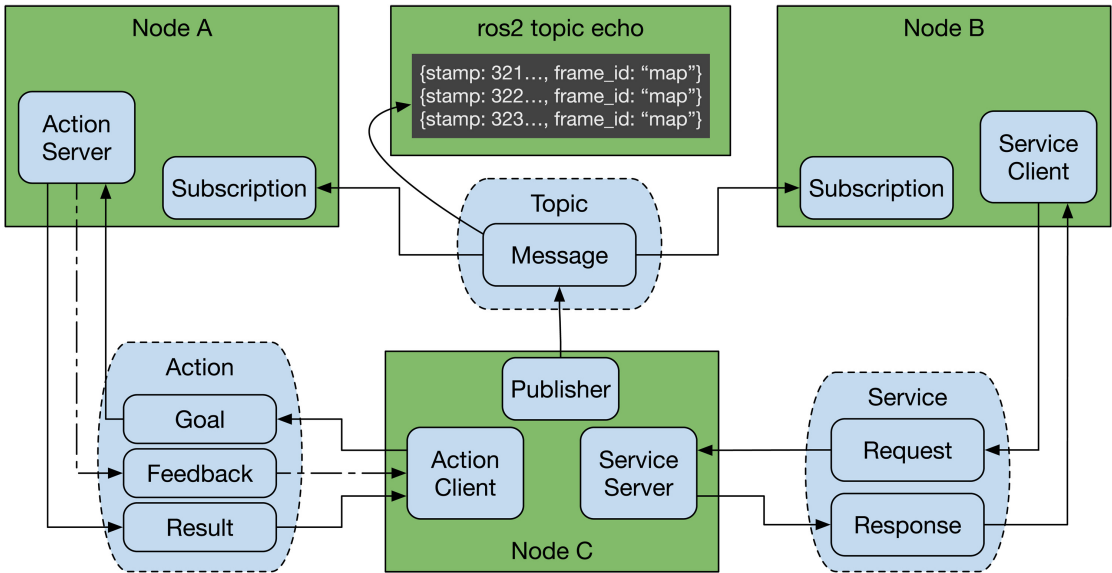


Figure 2.3.: An overview of a typical ROS 2 node network consisting of subscription nodes and publishing nodes, actions and service types can also be seen (Reprinted from [9] Fig 2)

2.4. Control Techniques in Robotic Surgery

Precise control, haptic feedback, complex system dynamics, and high safety standards drive the need for sophisticated control techniques in modern robotic surgery systems. Industry-leading platforms such as Intuitive Surgical's da Vinci system utilize Model Predictive Control (MPC) [10], enabling comprehensive modeling and prediction of system behavior. These systems also employ hierarchical control architectures (combining high-level planning with low-level execution) along with adaptive learning-based controllers to compensate for tissue deformation and operate effectively in dynamic environments.

Surgeon feedback is equally critical for successful surgical outcomes. Advanced haptic feedback and force control algorithms are implemented in MTMs to provide surgeons with precise tactile information [11]. Furthermore, real-time imaging and navigation systems deliver valuable intraoperative feedback to enhance surgical precision [12]. The

integration of artificial intelligence has revolutionized surgical robotics in recent years. Deep learning approaches now enable advanced perception and decision-making capabilities within these systems. For instance, real-time tissue identification [13] allows for dynamic force modeling, enabling systems to adapt intelligently to varying tissue properties during procedures.

2.5. System Identification Techniques in Robotic Surgery

Implementing advanced control strategies requires a dynamic understanding of system behavior, which can only be achieved through robust system identification. The highly nonlinear nature of many robotic systems demands excitation methods that remain effective under nonlinear conditions. Multisine and chirp signals form the basis for many modern system identification techniques [14], and are increasingly combined with reinforcement learning approaches [15]. In surgical robotics, where safety is paramount, a multi-stage identification process is critical. For example, Intuitive Surgical performs low-level actuator characterization using step-response tests to validate settling time, overshoot, and stiffness in every motor and joint. These physics-based models are then enhanced with AI/ML layers to handle complex surgical interactions. This hybrid approach delivers uncompromising system dynamics and performance [16].

2.6. Summary and Research Motivation

Modern robotic-assisted surgical systems provide a powerful framework to assist doctors and surgeons, enabling them to improve patient quality of care while reducing post-operative recovery time. While these systems are incredibly capable, their high cost and barriers to entry have limited accessibility for researchers. This limitation has led to the development of several lower-cost alternatives, such as the Da Vinci Research Kit, Raven II, and the Desktop Surgical System.

These systems inherit many features found in commercial solutions, including a ROS-based architecture and advanced control and identification techniques. However, the gap between their implementation and the current state of the art remains apparent. This research aims to reduce this technical gap by, upgrading the software architecture to ROS 2, implementing more advanced system identification techniques, and incorporating adaptive control to improve system performance.

3. Desktop Teleoperated Surgical Training System

In an effort to further advance the field of robotic-assisted surgery, researchers at MCI have developed a Desktop Teleoperated Surgical Training System[17]. The system's design was heavily inspired by the dVRK and Raven II, while trying to maximize performance and minimize cost. Because this system serves as the foundation for the research in this paper, and in depth understanding and exploration of this system is required.

3.1. Overall System Architecture

The system consists of two main components, the MTM and the PSM.

While the system was designed to include both left and right MTMs and PSMs. The complexities associated with the construction of control of both sides these systems lead to a reduction in the research scope to only one side of the system. Consequently, only one MTM and one PSM were manufactured and developed.

The MTM measures the operator's motion and communicates it to the PSM, which then replicates the movements. These individual systems will be explored further in the following sections, and an overview of the system can be seen in Figure 3.1.

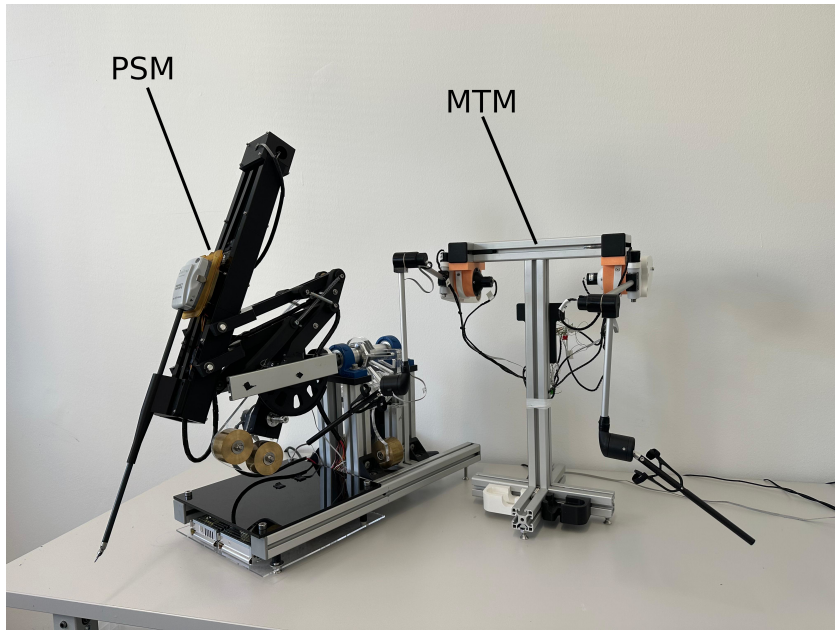


Figure 3.1.: Overview of the Desktop Teleoperated Surgical Training System, illustrating the MTM and PSM components.

3.1.1. MTM Overview

The MTM measures the operator's motion through a 7-DOF linkage, actuated by the user. The associated DOFs and their types are indicated in Table 3.1.

Table 3.1.: MTM Joint Classification and Positional Sensing.

Joint Classification	Dof Name	Positional sensing
Overall system positioning	J0	
	J1	12-bit absolute magnetic encoder
	J2	
Instrument positioning	G0	Hall Effect Sensor
	G1	
	G2	Analog Potentiometer
	G3	

These joints allow the operator to communicate desired motions to the PSM. The J0–J2 DOFs dictate the endpoint position, while G0–G3 control endpoint orientation and state.

The MTM should allow for accurate interpretation of the operator's intended motion while also minimizing the force perceived by the operator. This perceived force requirement drove the design toward a gravity compensation system (GCS).

An overview of the MTM with indications to the specific DOFs can be seen in Figure 3.2.

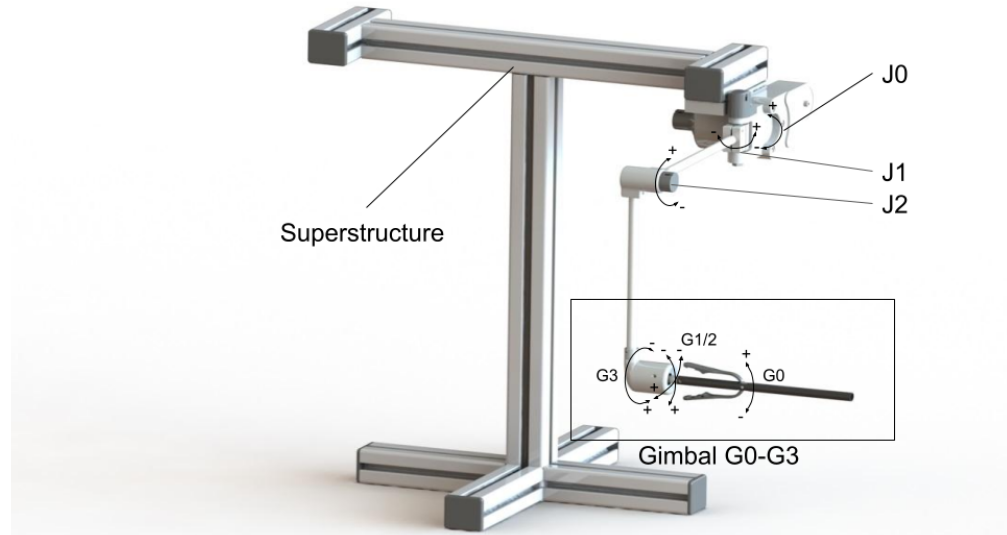


Figure 3.2.: Overview of the MTM with indicated DOFs.

3.1.2. PSM Overview

The PSM has 7 primary DOFs, classified as shown in Table 3.2.

Table 3.2.: PSM Joint Classification and Drive System.

Joint Class	DOF Name	Drive Type	Positional sensing
Overall system positioning	Roll Pitch Insertion	Brushless DC Motor	12-bit absolute magnetic encoders
Instrument positioning	Instrument Roll Instrument Pitch Instrument Tilt Instrument Grasp	Servo Motor	Servo feedback

An overview of the system with indications to the specific DOFs can be seen in Figure 3.3.

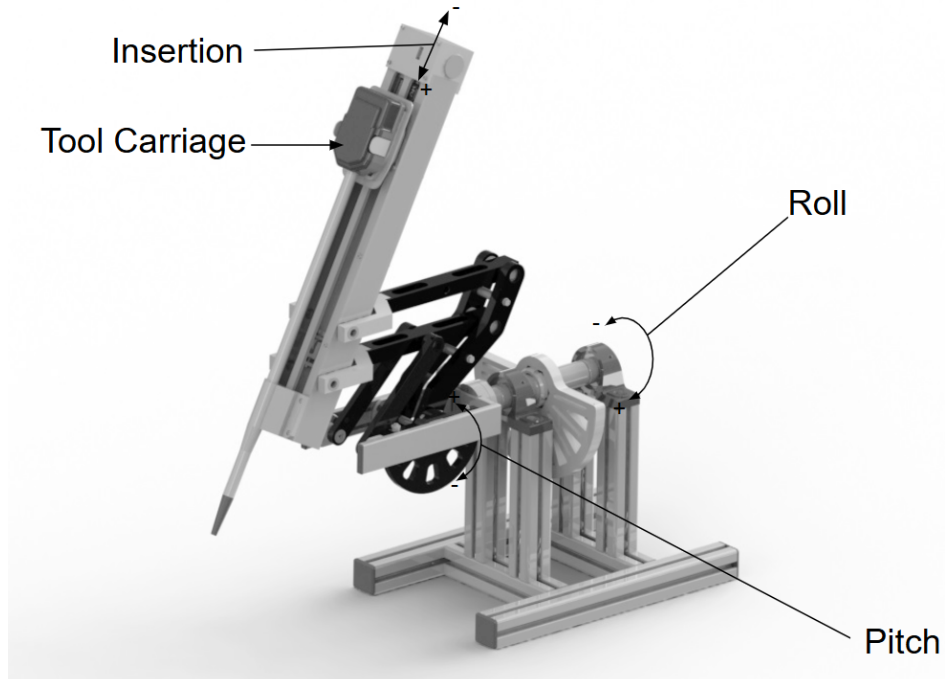


Figure 3.3.: Overview of the PSM with indicated DOFs.

3.2. MTM Mechanical Design

The MTM mechanical design can be separated into three subsystems, the arm (J0-J2), the gimbal (G0-G3), and the superstructure.

The arm subsystem is the primary architecture responsible for measuring the operator's position relative to the global reference frame. Three revolute joints with internal absolute magnetic encoders are coupled via rigid aluminum extrusions, allowing accurate estimation of the overall system positioning in 3D space.

The Gimbal subsystem, which is responsible for measuring the desired surgical instrument inputs, is a self-contained, 4-axis analog sensing apparatus. A 3D-printed shell contains the necessary analog sensing devices for determining the desired wrist position.

The superstructure is an aluminum extrusion structure that offsets the arm and gimbal subsystems from the table to allow space for manipulation.

3.2.1. Superstructure Design

The superstructure design is relatively straightforward. With no moving parts, it is purely designed to offer a platform on which the more complicated mechanics of the MTM can be mounted.

Several pieces of 20mm x 20mm aluminum extrusion are bolted together, offering a stable and modular platform. Previously, a 3D-printed piece held an Arduino Mega at the top of the superstructure, but this was updated to hold a Teensy 4.1 on the main superstructure beam to allow for easier access and wiring.

3.2.2. Arm Joint Design

The arm joints of the MTM feature relatively straightforward designs. The arm subsystem is rigidly coupled to the superstructure with a 3D-printed block, to which the origin of the arm's J0 joint is connected. Each joint is a simple revolute joint, directly coupled to an EAT-6012-A06 12-bit absolute magnetic encoders. These joints are then rigidly connected to each other through aluminum tubing, held in place by set screws. A detailed exploration of the J1 joint can be seen in Figure 3.4.

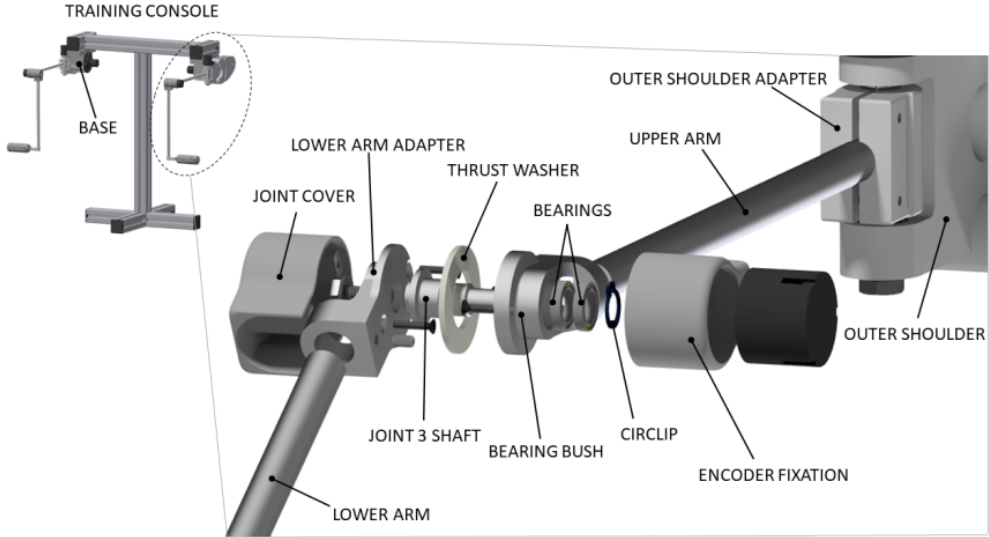


Figure 3.4.: Detailed view of the MTM's J1 joint design (Reprinted from [17] Fig 2.1)

The design of these joints was driven by the requirement to minimize friction. Increased frictional forces in any of these joints would result in an increase in perceived force by the operator. Roller bearings were utilized to minimize these frictional forces, and system mass was also reduced to lower both gravitational and inertial forces felt by the operator. However, in an effort to completely minimize forces felt by the operator, a GCS was implemented into the J0 joint.

The GCS consists of a brass cylinder, carefully massed to offset the gravitational forces felt by the system. The exact placement and mass of this cylinder were algorithmically determined in [17]. A detailed view of the mechanical design of this system can be seen in Figure 3.5.

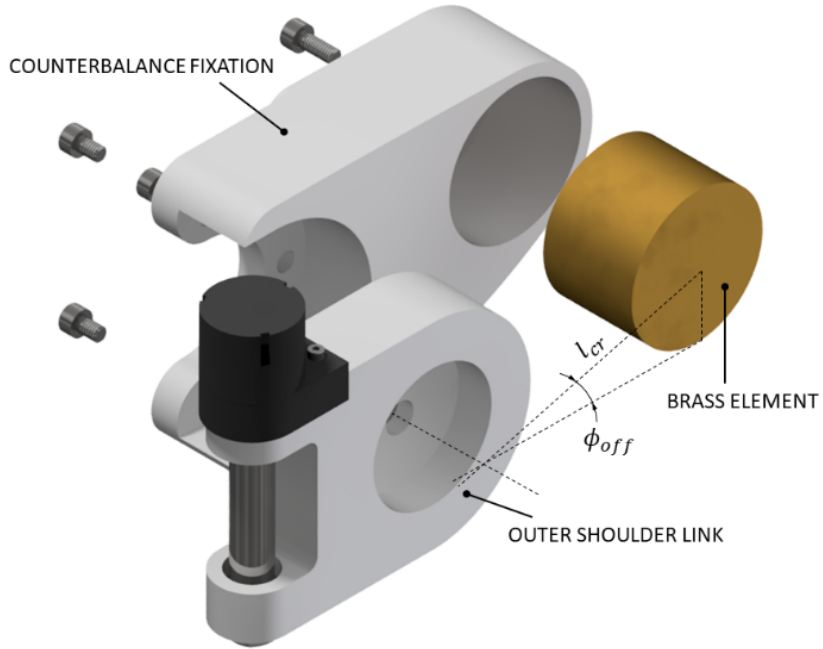


Figure 3.5.: Detailed overview of the MTM's GCS design. (Reprinted from [17] Fig 2.9)

3.3. MTM Electrical Architecture

3.3.1. System Overview

The MTM electrical architecture was originally based on an Arduino Mega 2560 microcontroller. This was later upgraded to a Teensy 4.1 microcontroller due to its compatibility with ROS2 and micro-ROS frameworks. Each DOF of the MTM is equipped with its own independent sensor for full positional sensing.

3.3.2. Joint Subsystems

Joints J0-J2 use AEAT-6012-A06 12-bit absolute magnetic encoders coupled to each joint axis for positional sensing. These encoders provide a theoretical positional accuracy of $\pm 0.088^\circ$ per joint. The encoder signals are sent to the Teensy 4.1's digital I/O pins and are supplied 5V power directly from the Teensy 4.1.

3.3.3. Gimbal Subsystem

The gimbal design changed drastically throughout the research. Initially, it utilized an MPU-6050 3-DOF IMU coupled with a Hall effect sensor for positional sensing [18]. However, during the course of this research, this subsystem was updated to replace the IMU with a series of three potentiometers coupled to a Hall effect sensor. G0 is measured using a Hall effect sensor on a lever arm linkage. This is then coupled to a modified FJN10K-C0 two-axis joystick potentiometer, which handles the angular sensing of G1 and G2. This joystick is coupled to the G3 potentiometer through a 3D-printed linkage. G0 used a SS495A Hall Effect Sensor, G1/G2 used a FJN10K-C0 two-axis joystick potentiometer, and G3 used a 3382H-1-103 Potentiometer.

Each of these sensors is supplied 3.3V power from the Teensy 4.1, and their resultant analog signals are sent to the Teensy 4.1's analog input pins.

3.4. PSM Mechanical Design

3.4.1. Overview

The PSM mechanical architecture is a 7-degree-of-freedom robotic system designed to replicate surgical instrument movements with high precision. The design is fundamentally inspired by the da Vinci Surgical System's remote center of motion mechanism, which maintains a fixed pivot point at the surgical incision site - a critical feature for minimally invasive surgery. The PSM can be divided into five primary subsystems., Superstructure and base, Roll axis, Pitch axis, Insertion axis, and Tool cart and end effector.

3.4.2. Superstructure

The superstructure is constructed from 80/20 aluminum extrusion and serves as the base upon which the other components are mounted. The base of the superstructure also houses the necessary electronics for the control of the PSM.

3.4.3. Roll Axis

The roll axis implements a revolute joint providing $\pm 30^\circ$ of rotation about the vertical axis. The system rotates in two roller bearings attached to the superstructure with a bearing block. A laser-cut acrylic wheel serves as the capstan drive of the system and is clamped to the central shaft. This wheel is connected to a brushless DC motor via steel cabling, offering a 20:1 reduction in a zero-backlash setup. This shaft terminates in a forked aluminum extrusion structure, to which the pitch subsystem connects. A limit switch is attached to the superstructure to allow for zeroing of the system.

This design offered a simple way to achieve precise, zero-backlash performance in an easy-to-assemble and low-cost package. A detailed depiction of this subsystem can be seen in Figure 3.6.

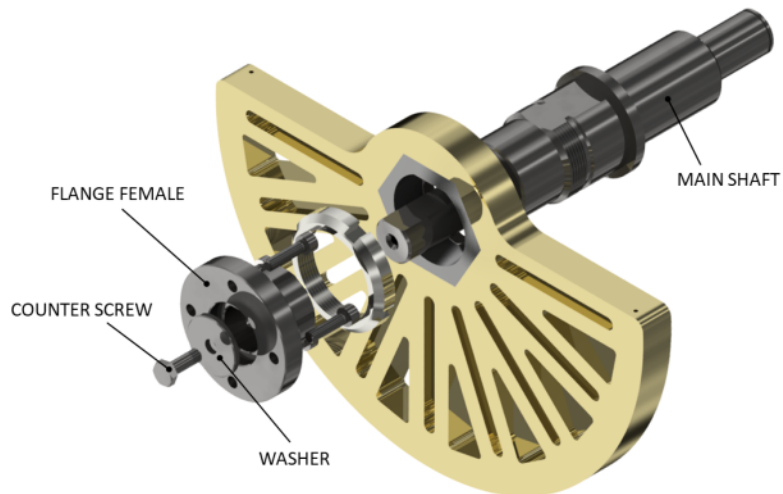


Figure 3.6.: Detailed view of the mechanical design of the roll axis, highlighting the main shaft design. (Reprinted from [17] Fig 2.10)

To minimize forces seen by the actuator, a gravity compensation system (GCS) was applied to this joint. This GCS consisted of two adjustable brass counterweights hanging directly below the capstan drive. Their mass and placement were once again algorithmically determined by previous research conducted by Walder [17]. A detailed view of the design of this GCS can be seen in Figure 3.7.

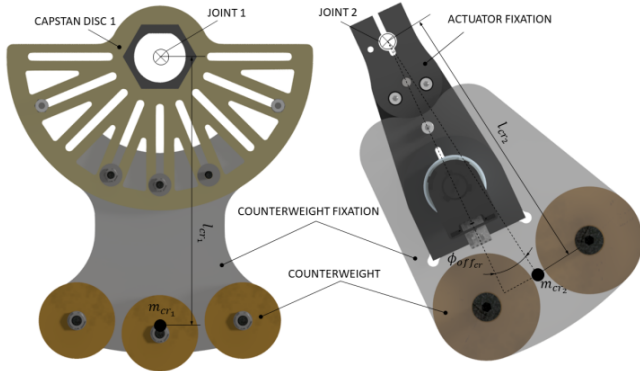


Figure 3.7.: A detailed view of the PSM's pitch and roll GCS design. (Reprinted from [17] Fig. 2.22)

3.4.4. Pitch Axis

The pitch axis replicates the Da Vinci's characteristic double parallelogram mechanism, which creates a virtual RCM distal to the joint. For ease of manufacturing, much of the PSM's pitch subsystem was designed to be 3D-printed, and for ease of assembly, many of the couplings were press-fits. This led to sagging of the mechanism and resulted in some of the linkages requiring maintenance during prolonged operation, but, overall, the linkage design was sound and maintained a remote center.

The pitch axis was coupled to the roll axis through the forked aluminum extrusion structure previously discussed in the PSM mechanical design section. Similar to the roll axis, the pitch axis was driven by a capstan drive system coupled to a brushless DC motor through steel cabling. A limit switch at the extreme limits of motion was once again used for zeroing the system, and the mechanism ultimately resulted in a $\pm 30^\circ$ range of motion. A detailed view of the pitch subsystem design can be seen in Figure 3.8.

Once again, a GCS was designed for the pitch subsystem. This design followed similar trends to the roll axis, placing a brass counterweight below the axis to reduce the force seen by the actuator. The design of this can be seen in Figure 3.7.

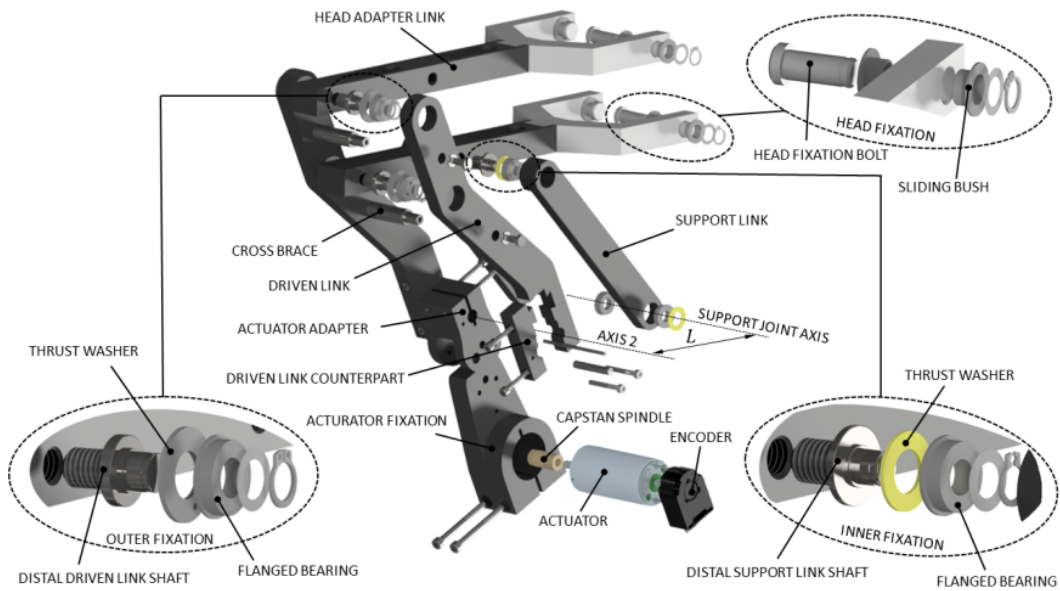


Figure 3.8.: Detailed view of the PSM's pitch axis mechanism. (Reprinted from [17] Fig 2.13)

3.4.5. Insertion Axis

The insertion axis design is relatively straightforward. A brushless DC motor coupled directly to a rack and pinion mechanism translates the rotary motion of the motor into the linear motion needed for the insertion axis. For ease of manufacturing, the majority of this mechanism was 3D-printed, and it was coupled to the pitch subsystem through a bolted connection via the end forks of the pitch linkage. For positional sensing, the carriage was coupled to an encoder through a belted connection. A detailed diagram of this subsystem can be seen in Figure 3.9.

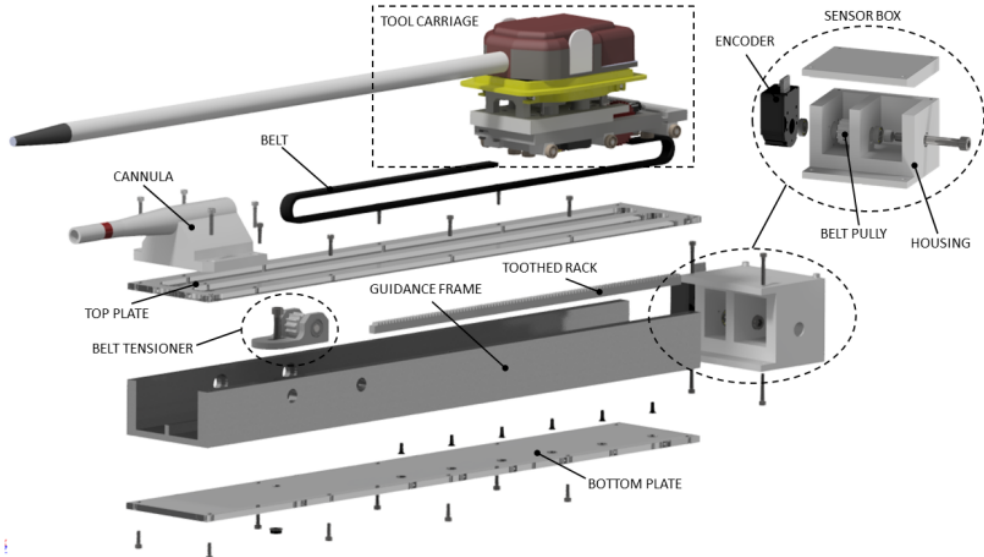


Figure 3.9.: Detailed view of the PSM's insertion axis mechanism. (Reprinted from [17] Fig 2.14)

3.4.6. Tool Cart and End Effector

The tool cart is responsible for driving the surgical instrument. This system uses off-the-shelf Intuitive Surgical instruments. These instruments are driven by a belted disc mechanism internal to the instrument. The tool cart houses four servo motors coupled to these discs with a spring-loaded compliance mechanism, as shown in Figure 3.10.

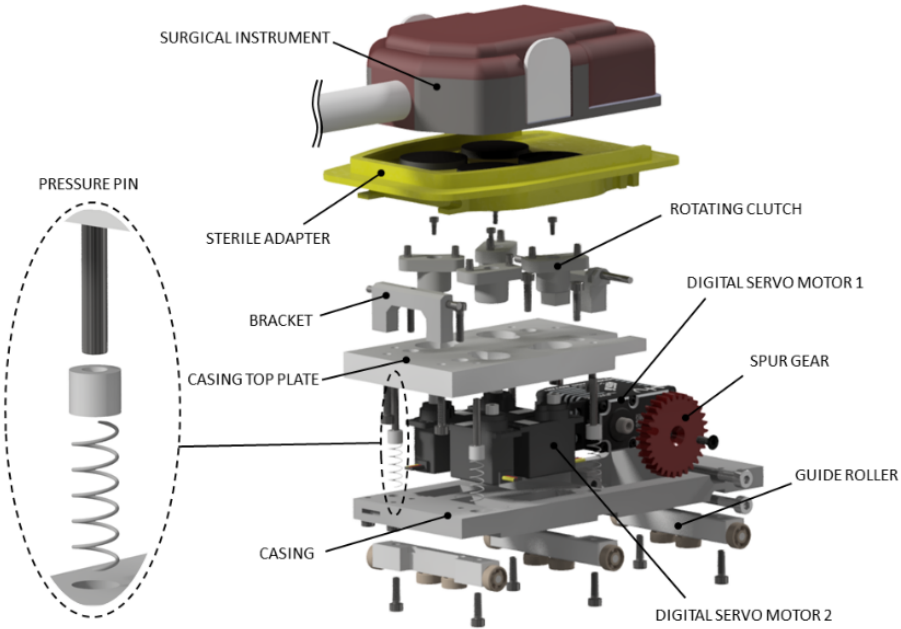


Figure 3.10.: Detailed view of the PSM's tool cart, highlighting the spring-loaded compliance mechanism. (Reprinted from [17] Fig 2.15)

3.5. PSM Electrical Architecture

The PSM electrical architecture is based on a Teensy 4.1 as the control unit of the system. Table 3.3 showcases each joint's associated electrical components.

Table 3.3.: PSM Joint Specifications

Joint	Drive Motor	Motor Driver	Positional Sensing
Pitch Roll Insertion	Maxon 273752 15V DC motor	MD13S Cytron 13 Amp	Broadcom HEDS-5540 encoder
Tool Roll Tool Tilt Tool Pitch Tool Grasp	MG966r Servo	None	Servo Feedback

3.6. System Software Architecture

As noted earlier in this paper, the initial software framework was implemented in an Arduino C-based environment. While the system has since been migrated to a ROS 2 architecture, the original implementation remains relevant for context and reference.

The software was divided into two primary components: the MTM software and the PSM software. These subsystems worked in tandem to enable real-time teleoperation, with the MTM capturing user inputs and the PSM replicating movements precisely.

3.6.1. MTM Software

The MTM software was responsible for several critical functions. Sensor data was read and processed from each of the DOFs associated sensors. Data was then filtered and converted into angular measurements based on predefined system parameters. Forward kinematics were then used to calculate the end effectors position based on angular measurements from sensors. Denavit-Hartenberg (DH) parameters were used for the forward kinematic calculations. All of the associated MTM data had to be parsed into a single serial string and output to the serial monitor for later acquisition by the PSM. In addition, sensor overflow was carefully monitored and spike detection logic was implemented to catch any spikes in sensor data. All relevant data had to be packaged with start/end markers for easy access and parsing by the PSM.

3.6.2. PSM Software

The PSM software was responsible for the control and drive of the PSM based on the movements of the MTM. Upon receiving target data from the MTM through the serial monitor the data had to be parsed and processed using a custom parsing function. The target position was then extracted from this data. Each joint was controlled through a PID control function with predetermined gains. Each joint had to be homed to its 0 position and the absolute encoder 0 value was also set through a ramp-up homing sequence in which the system carefully managed joint speed as it approaches the limit of motion. During operation limit switch state was monitored to ensure each joint was not colliding with the mechanical hard-stops. To ensure the surgical tool discs were engaged a tool catch procedure ran each servo through its complete range of motion and the PWM frequency was set to ensure that it lie outside of human range of hearing.

3.7. System Controller Design

Originally a PID controller was designed for the system using the Ziegler-Nichols method. This approach involved determining the critical gain (K_{cr}) and periodic time (P_{cr}) for each joint through root locus analysis. These values were then used with the McCormack tuning rules to calculate the initial PID constants, as presented in Table 3.4.

Table 3.4.: Initial PID Constants

Joint	Proportional gain (K_p)	Integral gain (K_i)	Derivative gain (K_d)
Roll	35.0	50.0	5.0
Pitch	60.0	110.0	15.0
Insertion	45.0	800.0	3.8

However, initial trials with these values resulted in unstable system motion and consistent undershoot[17]. As a result of these shortcomings, manual tuning of the PID coefficients was required to achieve satisfactory performance. However, even these manually tuned PID gains still resulted in unstable oscillations, particularly at the extreme ends of the range of motion. Consequently, the system was often operated using a simple P controller with manually selected gains, leading to very poor overall system performance.

3.8. System Kinematics and Coordinate Frames

It is critical to understand the system kinematics and coordinate frames for this system. This section will illustrate the defined coordinate frame positions with the system in its respect 0 positions.

3.8.1. MTM Coordinate Frame

As stated earlier, the MTM has 7 degrees of freedom. It is imperative to understand the coordinate frame of each of these axes. Figure 3.11 showcases each of these axes in their zero position with their respective coordinate frames attached. A detailed view of

the updated gimbal design with each of the axes in their zero position can be seen in Figure 3.12.

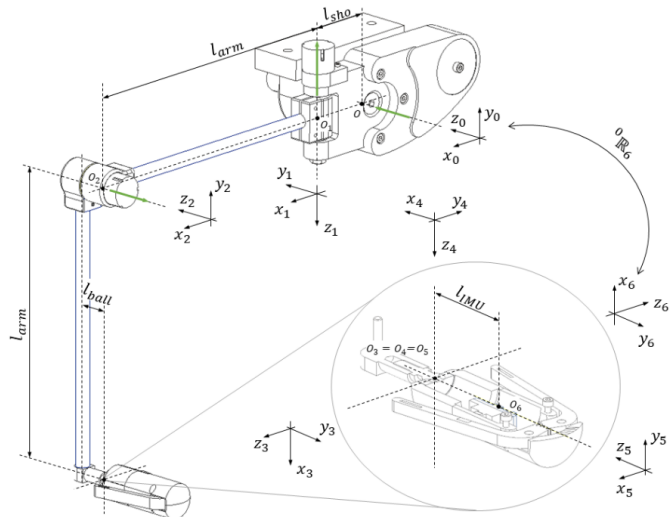


Figure 3.11.: The MTM and its associated degrees of freedom shown in their zero-position with DH-coordinate frames attached (Reprinted from [17] Fig 3.1)

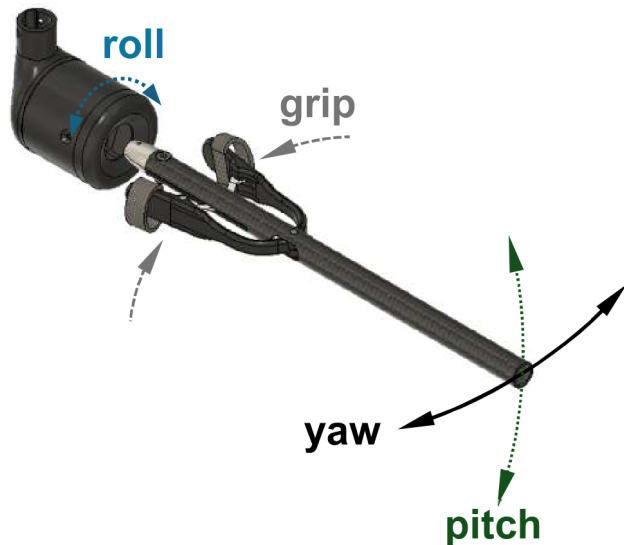


Figure 3.12.: The updated gimbal and its associated degrees of freedom shown in their zero-position. (Reprinted from [19] Fig 2.1)

3.8.2. PSM and Tool Coordinate Frame

The PSM and its associated tool have a total of 7 degrees of freedom. Each of these degrees of freedom can be seen in their zero position in **Figure 3.13.**

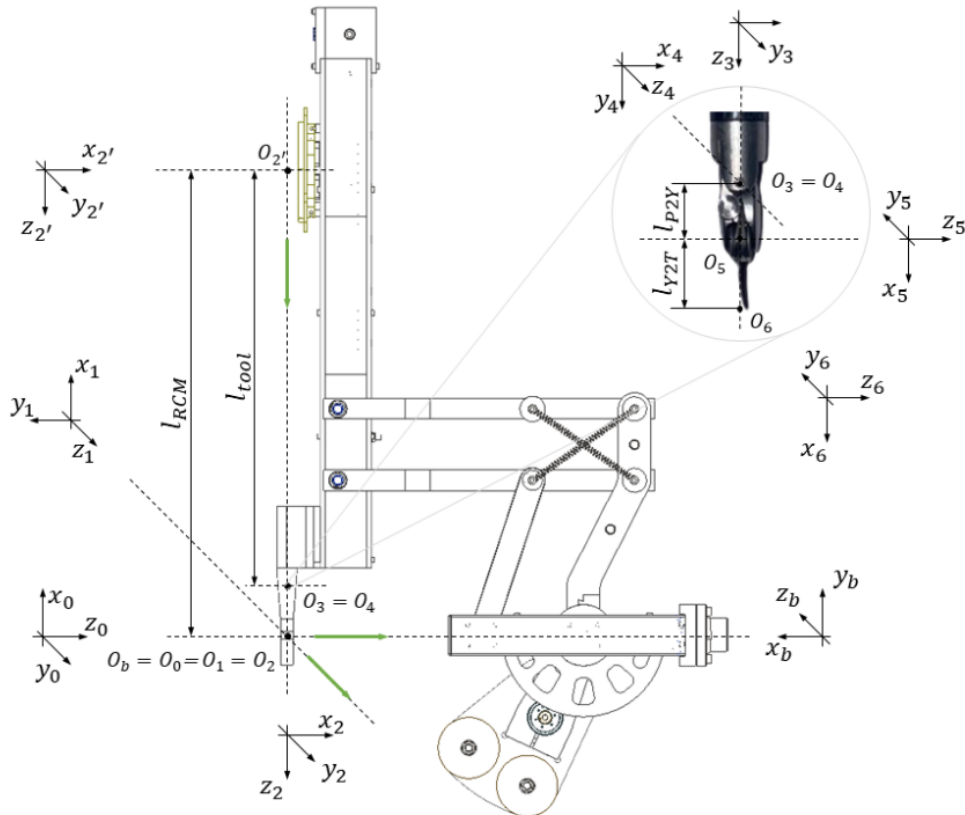


Figure 3.13.: The PSM and endowrist tool shown in their zero-position with DH-coordinate frames attached, according to the cDH convention. (Reprinted from [17] Fig 3.2)

4. Implementation on Current Hardware

4.1. Software Architecture

This section will serve as an overview of the current system software architecture and will provide an in-depth analysis of how the current ROS 2 Node structure works.

4.1.1. ROS 2 System Architecture

There were 4 main nodes in the systems ROS 2 design. The MTM node was responsible for streaming sensor data from the MTM, while also calculating joint angles and relaying these angles to the joint publisher node. The system model node consisted of an SDF model of the MTM allowing for visualization of the MTM's position. Additionally, target end effector position could be calculated from this model through frame transformations. The joint publisher node acted as intermediate between the SDF model and the ROS 2 workspace. It relayed the joint angles from the MTM to the SDF model and the target end effector position to the PSM node. Finally, the PSM node was responsible for the control and drive of the PSM. It also broadcasted PSM sensor data and joint states into the ROS2 workspace.

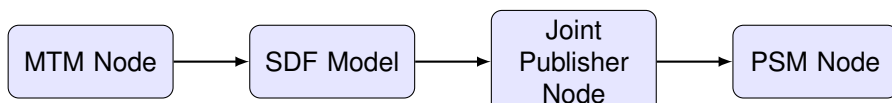


Figure 4.1.: Initial ROS 2 System Architecture for Target Pose Calculation.

Initially, the research aimed for the MTM Node to relay its joint angles to the SDF Model of the MTM. Subsequently, the Joint Publisher Node would calculate the desired end-effector position via a TF frame transformation from the base frame to the gimbal origin. This approach eliminated the need for direct forward kinematic calculations. This architecture is illustrated in Figure 4.1. While this method proved effective in accurately calculating the target pose, real-time performance trials revealed significant limitations.

Specifically, while target position extracted from the model demonstrated excellent real-time performance, a communication issue was found when the Joint Publisher Node interfaced with the PSM Node. This breakdown was likely caused by memory limitations in the Teensy 4.1, leading to high latency and noticeable data stuttering.

As a result, a simplified architecture was briefly explored to try to prevent this issue. This approach directly calculated the target pose using forward kinematics in the MTM node and then directly relayed this to the PSM node. This simplification of the technical stack had the potential to increase real-time performance; however, it also increased the forward kinematics calculation complexity and eliminated the opportunity to use the SDF model for further research. This architecture is presented in Figure 4.2.

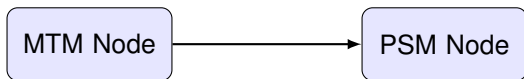


Figure 4.2.: Simplified ROS 2 System Architecture for Direct Target Pose Streaming.

Ultimately, this simplified architecture was not chosen. The elimination of the SDF model would result in limitation of future research resources and as a result the initial architecture was chosen, and further development efforts were undertaken to eliminate the data loss issues previously discussed.

4.1.2. MTM Modeling and Visualization

For the modeling of the MTM, the Simulation Description Format (SDF) was chosen due to its compatibility with ROS 2 and RViz. SDF also supports complex kinematic structures, including closed-chain kinematics, which is crucial for accurately modeling the more intricate four-bar style linkages found in the PSM.

Generating the SDF file proved to be a fairly involved process. First, the CAD model of the MTM system was imported into SolidWorks. To reduce computational complexity, the model underwent significant simplification. Parts were condensed into their respective links, identified as Base, J1 (Joint 1), J2 (Joint 2), J3 (Joint 3), G3 (Gimbal Link 3), G2 (Gimbal Link 2), G1 (Gimbal Link 1), and G0 (Gimbal Link 0). Each of these components was created as a singular solid part and then reassembled within SolidWorks into a complete assembly.

Following this, rotational axes and origins were assigned for each link. A SolidWorks plugin was then utilized to export the model into a Universal Robot Description For-

mat (URDF) file [20]. This URDF file was subsequently converted to SDF using `ros2_sdf_to_urdf` [21]. Upon the successful generation of the SDF model, a Python launch file was developed to facilitate quick and easy visualization of this model within RViz.

The final result of this effort can be seen below in Figure 4.3.

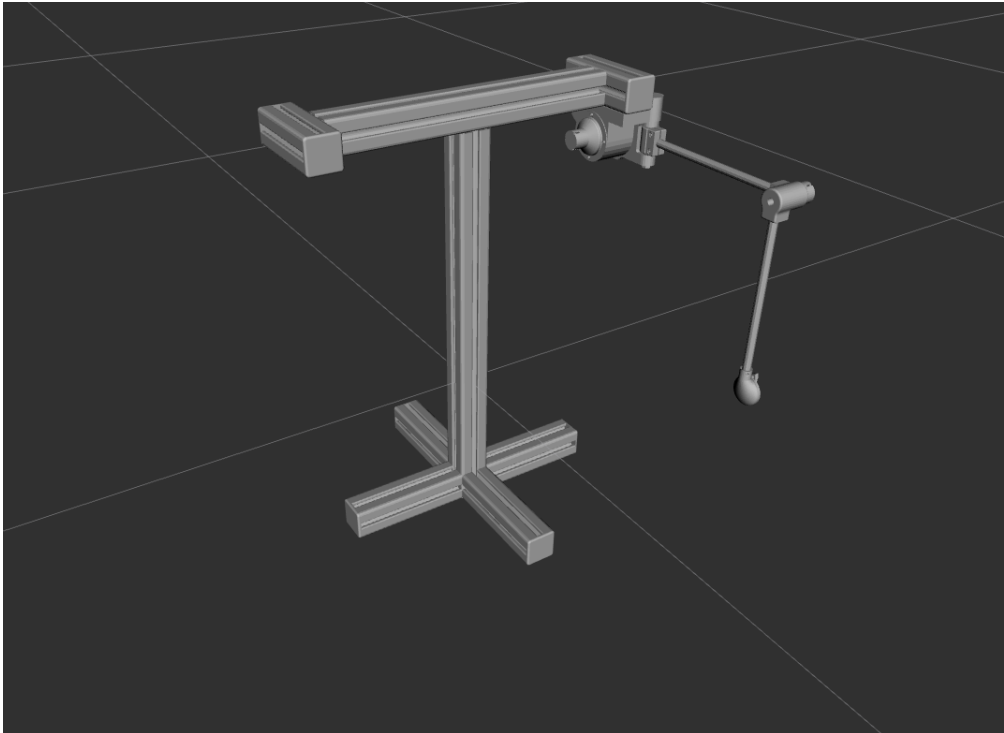


Figure 4.3.: SDF model of MTM shown in the RViz environment. The gimbal solid models have been hidden in this model

4.1.3. MicroROS Implementation

Since the teensy 4.1 does not support the full ROS 2 stack, MicroROS was utilized to allow the microcontroller to communicate with the ROS 2 system. MicroROS is a lightweight version of ROS 2 designed for microcontrollers and resource-constrained devices. It provides a subset of the ROS 2 features, enabling communication between nodes while maintaining low memory and processing overhead.

In order to set up MicroROS on the Teensy 4.1, the following procedure was implemented in both the MTM and PSM nodes to initialize the MicroROS environment:

First the necessary Micro-ROS header was included

```
1 #include <micro_ros_platformio.h>
```

Listing 4.1: Include Micro-ROS PlatformIO Header

Next, the serial port was configured as the communication transport for Micro-ROS.

```
Serial.begin(921600);
set_microros_serial_transports(Serial);
delay(2000); // Give time for connection to establish
```

Listing 4.2: Set Micro-ROS Serial Transport

The default allocator was obtained and used for memory management.

```
allocator = rcl_get_default_allocator();
```

Listing 4.3: Initialize Micro-ROS Allocator

The `rclc_support_init` function initialized the Micro-ROS support structure, which is a key ROS 2 component

```
RCCHECK(rclc_support_init(&support, 0, NULL, &allocator));
```

Listing 4.4: Initialize Micro-ROS Support Structure

Next a ROS 2 node was created

```
RCCHECK(rclc_node_init_default(&node, "mtm_arm_node", "", &support));
```

Listing 4.5: Initialize ROS 2 Node

All necessary publisher were created to send messages on specified topics

```
RCCHECK(rclc_publisher_init_default(
    &joint_state_publisher,
    &node,
    ROSIDL_GET_MSG_TYPE_SUPPORT(sensor_msgs, msg, JointState),
    "mtm_joint_states"));
```

Listing 4.6: Initialize Micro-ROS Publishers

Finally, the Micro-ROS executor was initialized. The executor is responsible for managing the execution of callbacks associated with subscriptions, timers, and other ROS 2 entities.

```
RCCHECK(rclc_executor_init(&executor, &support.context, 1, &allocator));
```

Listing 4.7: Initialize Micro-ROS Executor

After the Micro-ROS node is initialized and running on the embedded device, a Micro-ROS agent on the Linux machine can be started

```
ros2 run micro_ros_agent micro_ros_agent serial --dev /dev/ttyACM0
```

Listing 4.8: Run Micro-ROS Agent Command

4.1.4. MTM Data Streaming and filtering

The MTM node's primary purpose is to process incoming sensor data and broadcast it into the ROS2 workspace in a usable format. The following topics are published into the ROS2 workspace from the MTM:

Table 4.1.: MTM ROS2 Topics

Topic Name	Topic Type	Description
mtm_joint_states	sensor_msgs/msg/JointState	Current angular positions for all robotic arm joints.
mtm_raw_values	std_msgs/msg/Float32MultiArray	Unfiltered raw sensor data for debugging.
target_pose	sensor_msgs/msg/JointState	Calculated Cartesian (x, y, z) position of the end-effector in meters.

It was noticed initially that the `mtm_joint_state` topic had quite noisy data, resulting in jitter in the systems that subscribed to this topic. As a result, a simple low-pass filter with an alpha value of 0.1 was applied to this data before being published. This significantly reduced noise in the published signal and greatly improved system performance.

4.1.5. MTM to PSM Communication Protocol

As previously established in Section 4.1, there are two separate paths for data communication between the MTM and the PSM: the direct communication path and the path

utilizing the SDF model as an intermediary.

A critical aspect of both communication paths is ensuring **Quality of Service (QoS)** protocol matching. QoS allows for the definition of how topics are communicated between nodes. Ensuring that communicating nodes utilize appropriate and compatible QoS protocols is essential for software reliability and robustness. For this research, the QoS reliability and queue depth were modified to ensure proper message delivery.

Initially, an issue arose with the communication protocol between the SDF model and the PSM node. Data streamed from the SDF model was published to the `/model_pose` topic. When this data was plotted, it exhibited high quality with zero latency or lag. However, when the PSM topic `/psm_joint_telemetry` subscribed to `/model_pose`, a significant loss of data occurred, resulting in lag and stuttering. This led to unacceptable system performance. After extensive diagnostics, the data performance was improved by drastically increasing the publishing rate from 100 Hz to 1000 Hz, increasing the queue depth from 10 to 20, and applying a custom QoS profile:

Increasing the publishing rate to such a drastic level required careful memory consideration to avoid overwhelming the limited memory of the PSM's Teensy 4.1. As a result, the `model_pose` message type was changed from a `JointTelemetry` message type to a `JointState` message type to reduce memory strain.

The specific implementation of the QoS profile can be seen in the following code:

```
rmw_qos_profile_t custom_qos = {  
    RMW_QOS_POLICY_HISTORY_KEEP_LAST, // history  
    15, // depth (queue size)  
4    RMW_QOS_POLICY_RELIABILITY_RELIABLE, // reliability  
    RMW_QOS_POLICY_DURABILITY_VOLATILE, // durability  
    {0, 0}, // deadline (rmw_time_t sec, nsec)  
    {0, 0}, // lifespan  
    RMW_QOS_POLICY_LIVELINESS_SYSTEM_DEFAULT, // liveliness  
9    {0, 0}, // liveliness lease duration  
    false // avoid_ros_namespace_conventions  
};
```

Listing 4.9: Custom QoS Profile Definition

4.1.6. PSM Software

The PSM software node's primary responsibility is the control of the physical PSM system. While this task may appear simple on the surface, its implementation was quite complex, requiring several different software components to work together cohesively.

The PSM node had three primary modes. In Target mode, the PSM node received target joint angles from the MTM node and the Joint Publisher Node. The PSM would then drive the system to these target angles using a control algorithm. This mode was primarily used for the normal operation of the PSM. In sin mode the PSM followed a sinusoidal trajectory to verify the system's performance. This mode was primarily used for testing and validation purposes in the case of smooth, predictable motion. In trajectory mode PSM followed a predefined trajectory path generated by moving the MTM. This was used to verify the PSM performance between control strategies across a consistent, real-world desired trajectory.

The mode was defined in the beginning of the script with the String variable `control_mode`. In these modes, the primary codebase remained the same, consisting of a `main.cpp` file and multiple helper files. The main difference between the modes was how the desired target position was generated. In Target Mode, the PSM node subscribed to the `/mtm_target_pose` topic. In Sin Mode, it generated a sinusoidal joint angle trajectory based on predetermined amplitude and period parameters. In Trajectory Mode, the MTM was used to generate a trajectory path, which was then stored as a list in a header file for the PSM to parse as a series of desired target positions.

Sin and Trajectory mode were only intended to be verification modes used to verify the performance of the control algorithms for the pitch and roll joints. As a result, the tool was left undriven in these modes and only the overall x,y,z target was considered.

In Target Mode, the tool positioning was considered and as a result the PSM node subscribed to two different topics. For overall positioning of the system, it subscribed to the `/target_pose` topic generated by the Joint Publisher Node. This topic provided the target position in an x, y, z format. The PSM node then used this target position to calculate the necessary joint angles to achieve this position. Additionally, to determine the desired tool angles, it subscribed to the `/mtm_joint_states` topic. This topic provided the current gimbal angles of the MTM system, which were used to calculate the necessary joint angles for the PSM system.

The actual calculation of the desired joint angles differed across the operational modes.

In Sine Mode, the generated trajectory was already in the form of joint angles, allowing the joints to be directly commanded to their desired position without further calculation.

For both Trajectory Mode and Target Mode, additional calculations were required to convert the intended (x, y, z) target position to the actual desired joint angles. For this calculation, the function `computePSMJointAngles`, contained within the auxiliary file `psm_compute_joint_angles.cpp`, was used. This function took an (x, y, z) target position as input and returned a custom structure `JointAngles` containing the desired joint angles. The following demonstrates the mathematics behind this calculation.

x, y, z are the Cartesian coordinates of the target position. The joint angles are defined as:

- **Insertion Distance (q_3):** This is the Euclidean distance from the origin to the target point, representing the linear extension of the insertion joint.

$$q_3 = \sqrt{x^2 + y^2 + z^2}$$

- **Pitch Angle (q_2):** This angle is derived from the x and y coordinates representing the roll angle.

$$q_2 = \frac{1}{4} \arctan(x, y)$$

The result is then constrained within $[-30^\circ, 30^\circ]$.

- **Yaw Angle (q_1):** This angle is derived from the z and y coordinates, representing the pitch angle.

$$q_1 = -\frac{1}{4} \arctan(z, y)$$

The result is then constrained within $[-30^\circ, 30^\circ]$.

The actual implementation of these calculations can be seen in the following C++ code snippet:

```

// Function to compute PSM joint angles from Cartesian coordinates
JointAngles computePSMJointAngles(double x, double y, double z) {
    JointAngles angles;
    // Compute insertion distance (q3) as the Euclidean distance
    angles.q3 = static_cast<float>(std::sqrt(x * x + y * y + z * z));
    // Compute pitch angle (q2) in degrees and constrain
    double pitch = (std::atan2(x, y) * 180.0 / M_PI) / 4.0;
    pitch = constrain_value(pitch, -30.0, 30.0); // Assuming
        constrain_value is defined
    angles.q2 = static_cast<float>(pitch);
    // Compute yaw angle (q1) in degrees and constrain
    double yaw = -(std::atan2(z, y) * 180.0 / M_PI) / 4.0;
    yaw = constrain_value(yaw, -30.0, 30.0); // Assuming constrain_value is
        defined
    angles.q1 = static_cast<float>(yaw);
    return angles;
}

```

Listing 4.10: C++ Function for Joint Angle Calculation

The PSM software stack was quite extensive and, as a result, was broken up into several components to improve readability and debugging. These software subcomponents and their description can be seen in Table 4.2**.

Table 4.2.: Overview of Primary Files in the PSM Software Codebase

.cpp File Name	Purpose
config.h	Central repository for all configuration parameters and variables.
LQR.cpp	LQR and LQI control algorithms.
PID.cpp	PID control algorithm.
axis_conversion.cpp	Converts axis encoder counts to angular value.
encoder_reader.cpp	Reads raw encoder data.
gain_schedule.cpp	Gain scheduling algorithm and interpolation for control scheme.
helper_functions.cpp	Various helper and utility functions.
homing.cpp	Homing sequence and logic.
main.cpp	Main entry point tying all other files together.
psm_joint_angles.cpp	Joint angle calculation of PSM based off target position.

4.2. System Identification

For this research, proper controller design was paramount. However, a high-performance controller could not be designed without a fundamental understanding of the system's dynamics. To achieve this, a robust system identification scheme was developed.

The two primary joints of interest were the roll and pitch joints. These joints exhibited complex system dynamics and a high degree of nonlinearity. An exact system identification approach was tailored to each joint's unique dynamics.

4.2.1. Roll Joint Open Loop Step Response

The roll joint can be mechanically described as a pendulum. Perturbations applied to the system move the joint away from its 0° position, but when the perturbation ceases, gravitational forces return the joint to its 0° position. The system was also determined to have a fairly consistent and predictable transfer function. Specifically, when the brushless motor was driven at a specific voltage, the resulting positional change of the system was consistent across trials. As a result of these factors, a step response characterization was deemed an excellent method for system identification.

A step response characterization is a common system identification method in control engineering. In this technique, the system's input is abruptly changed from one value to another, and the resulting system response is measured and used to characterize the system's dynamics.

For the roll axis, a very lightly tuned PID controller was initially employed to drive the system to the intended point of characterization. A predetermined delay allowed the system to settle into a stable state. Upon completion of this delay, the current motor voltage value was stored, then scaled by a factor of 1.1 before being sent to the motor. Both the motor voltage input over time and the positional output of the roll joint over time were recorded. This system response data was saved as a CSV file and subsequently loaded using a custom MATLAB script. This script parsed the data and then fitted a second-order transfer function to the system response using MATLAB's `tfe` command. Finally, state-space matrices could then be extracted from this transfer function using MATLAB's `ss` command.

4.2.2. Closed Loop Excitation Through PRBS

Initial characterization of the pitch subsystem used a similar approach to the roll subsystem. A step response was applied, and the resulting response was used to characterize the system. However, several issues were found with the step response characterization of the pitch subsystem.

Due to the mechanical nature of the joint, the pitch subsystem's response was highly nonlinear. A slight change in voltage applied to the motor resulted in large changes in the pitch system's position, and this behavior was not consistent between trials. The same change in motor voltage would not result in the same system response. Additionally, when a small increase in voltage was applied to a stable system position, the pitch subsystem would drive to the end of its range of motion and contact the hard stop. This overshooting was a result of the pitch subsystem's extremely sensitive system response as its angle increased. This sensitivity was a direct consequence of the mechanical design of the pitch subsystem, where the force applied by the gravity compensation system drastically reduced as the angle of the pitch subsystem increased.

As a result of these complexities, a different approach had to be implemented. Due to the difficulties in maintaining the pitch subsystem within its intended range of motion, it was deduced that system identification needed to be conducted under closed-loop system control.

For this system identification technique, a light PD controller was applied to the system. The system was then commanded to its intended characterization point. Upon a predetermined settling time, the control input was then excited with a Pseudo-Random Binary Sequence (PRBS).

PRBS is a control signal excitation technique in which the control input is randomly fluctuated by a set amplitude at pseudo-random, predetermined intervals [22]. By exciting the control input, the resulting behavior and system dynamics could be observed while the aforementioned PD controller attempted to bring the system back to its setpoint. Key considerations in closed-loop PRBS excitation are ensuring that the amplitude of the excitation is sufficient to bring the system off its setpoint and overcome noise, while also ensuring that the amplitude of the excitation does not overpower the controller and drive the system off its setpoint. Additionally, the intervals between the fluctuations of the excitation need to be chosen such that the system's dynamics are excited across a variety of frequencies.

To ensure that the system undergoes excitation at all critical frequencies multiple times, the PRBS characterization was run for an extended period. Trials typically lasted 30-660 seconds. During these trials, the pitch subsystem's input voltage and resulting position were continuously recorded. This output data was saved as a CSV file, and an additional MATLAB script was used to perform a mathematical characterization of the system.

Similarly to the roll subsystem, the recorded output of the pitch subsystem was loaded into a MATLAB script, and a variety of system identification techniques were applied to the data.

From these results, it was determined that a 4th-order transfer function estimation was the best method for characterizing the system.

After a 4th-order transfer function was fitted to the system using the MATLAB `tfest` command, the state-space matrices were extracted using the `ss` command. The estimated model's accuracy was then determined by comparing the actual system behavior based on the input to the predicted system behavior based on the system input using the MATLAB `compare` command.

From this comparison, it was determined that the model accuracy was quite low when compared to the real system response based on the input. However, when a controller was designed around this model estimation, the actual systems positional error remained less than 1 degree in both joints on average. So, while this poor system estimation may point towards some underlying issues in the system identification technique, it ultimately resulted in a high-performing controller, which was the ultimate goal of this research.

4.2.3. Multi-point System Identification

Due to the kinematics of the system, the force required of the motors at various joint positions will vary. As the roll angle diverges farther from 0 in both the negative and positive direction, there is an increase in gravitational forces seen by the actuators, and as a result, the voltage applied to the motor would need to be increased accordingly. This trend is theoretically illustrated in Figure 4.4.

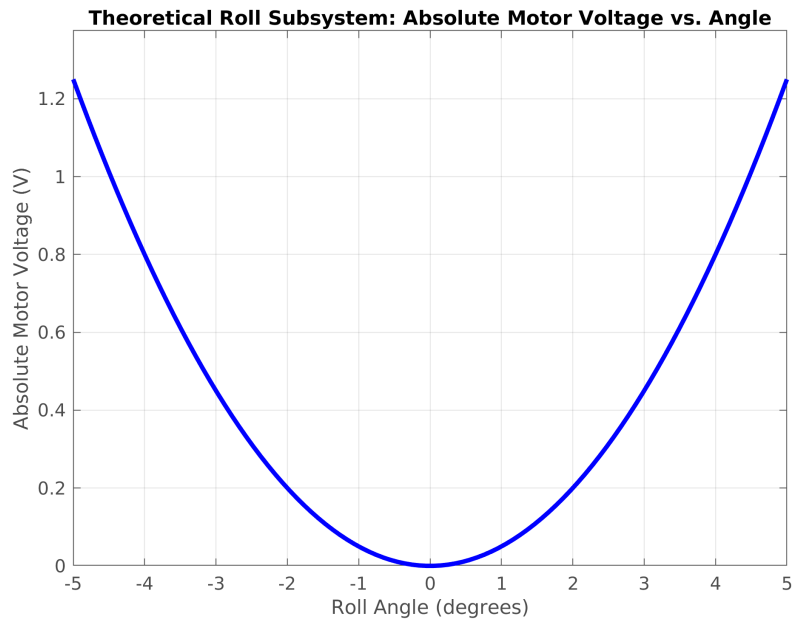


Figure 4.4.: Theoretical trend of absolute motor voltage required for the roll subsystem as a function of roll angle.

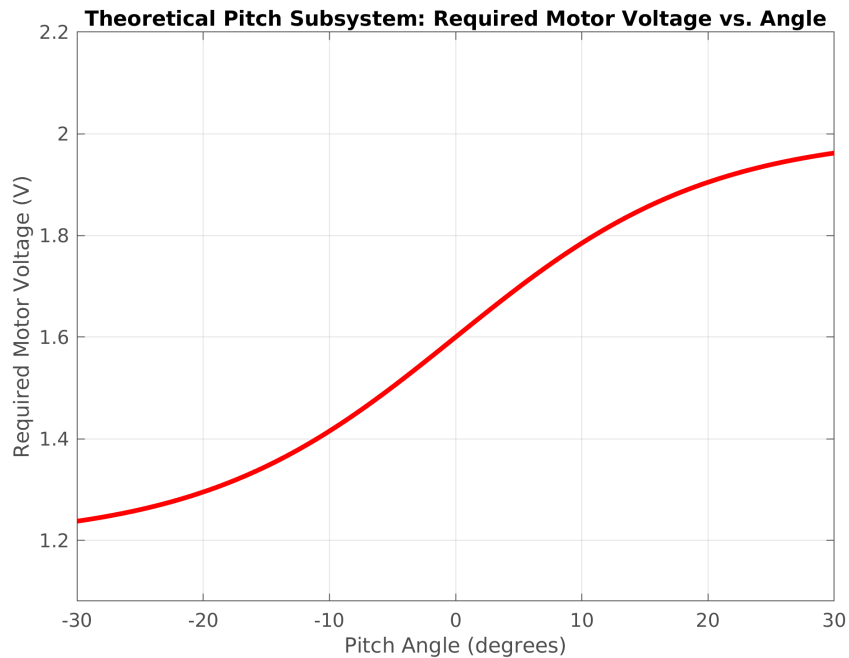


Figure 4.5.: Theoretical trend of required motor voltage for the pitch subsystem as a function of pitch angle.

For the pitch subsystem, the force required by the actuator actually decreases as the joint moves through its range of motion from -30 degrees to 30 degrees. The theoretical voltage required for the pitch subsystem across its range of motion is shown in Figure 4.5.

Additionally, complexities are added to the system dynamics when one realizes that the force required by the roll subsystem is also coupled to the pitch subsystem's position. As the pitch subsystem's angle is increased, the force required by the roll subsequently changes due to the system's center of mass changing position.

Similarly, the force required by the pitch subsystem varies with the position of the roll subsystem. As the roll subsystem diverges from the 0 point, the force required by the pitch subsystem lessens as it stays farther from its default position (normal to the gravitational force vector).

The combination of these factors necessitated the need for a more complex controller strategy in which the controller gains varied in accordance with the system position. The idea of this improved controller was that each joint's gains would vary with the current position of each subsystem.

This adaptive controller algorithm would require the characterization of the system at multiple points of the system's position. It was decided that 9 characterization points would be used for each joint of the subsystem. The pitch would be varied from -15° , 0° , 15° and the roll subsystem would vary from -20° , 0° , 20° . This resulted in the following grid of 9 characterization points:

Table 4.3.: Grid of 9 Characterization Points for System Identification

		Roll Angle ($^\circ$)		
		-20	0	20
Pitch Angle ($^\circ$)	-15	(-15, -20)	(-15, 0)	(-15, 20)
	0	(0, -20)	(0, 0)	(0, 20)
	15	(15, -20)	(15, 0)	(15, 20)

Once the necessary characterization points were established, the system needed to be identified at each of these points for each joint, resulting in the necessary system identification procedures. The actual system identification process was fairly straightforward. The previously established strategy for each joint was used; the only difference was that the positional setpoint for each characterization point varied to ensure the joint

not being characterized remained at the necessary setpoint. The controller designed around the (0, 0) characterization point was used. While it was found that the dynamic performance of the controller designed around the (0, 0) setpoint degraded as the system diverged farther from the original linearization point, this controller performed well enough in the case of a static setpoint that it could be used to hold the extreme angles required by the multi-point system identification.

Once the necessary characterization points were established, the system needed to be identified at each of these points for each joint, resulting in the necessary system identification procedures. The actual system identification process was fairly straightforward. The previously established strategy for each joint was used; the only difference was that the positional setpoint for each characterization point varied to ensure the joint not being characterized remained at the necessary setpoint. The controller designed around the (0, 0) characterization point was used. While it was found that the dynamic performance of the controller designed around the (0, 0) setpoint degraded as the system diverged farther from the original linearization point, this controller performed well enough in the case of a static setpoint that it could be used to hold the extreme angles required by the multi-point system identification.

Upon the completion of each system identification trial, the resulting system response was saved in a CSV file under the following format: IDENTIFIEDJOINT_ROLLANGLE_PITCHANGLE.csv. A MATLAB script was then used to parse each of these files, identify the system at that point, and store and plot the system identification results.

The specific implementation of the multi-point system identification for the roll joint is as follows:

Data Loading and Preprocessing The raw sensor data is loaded from a CSV file. For the Roll system, a step response is analyzed. The data is then trimmed to isolate the relevant section around the step change, and normalized by subtracting initial values to focus on the system's response to the step input.

```

% Read CSV file with preserved headers
roll_data = readtable('roll_step.csv', 'VariableNamingRule', 'preserve');
% Extract time and normalize
roll_time = roll_data.time - roll_data.time(1);
5 % Extract roll data using original column names
roll_position = roll_data.('roll_position');
roll_velocity = roll_data.('roll_velocity');
roll_effort = roll_data.('roll_effort');

10 % Find step change time and trim data
velocity_threshold = 0.1;
roll_step_idx = find(abs(diff(roll_velocity)) > velocity_threshold, 1);
roll_trim_idx = roll_step_idx:min(roll_step_idx+500, length(roll_time));

15 % Prepare data for system ID (normalize to start from zero)
roll_y = roll_position(roll_trim_idx) - roll_position(roll_trim_idx(1));
roll_t = roll_time(roll_trim_idx) - roll_time(roll_trim_idx(1));
roll_u = roll_velocity(roll_trim_idx) - roll_velocity(roll_trim_idx(1));

```

Listing 4.11: Roll Data Loading and Preprocessing

System Identification (Transfer Function Estimation) Next, a 2nd-order transfer function is estimated from the preprocessed input-output data using the `tfest` function. The `iddata` object encapsulates the input, output, and sampling time.

```

% Prepare data for system ID
2 roll_data_iddata = iddata(roll_y, roll_u, mean(diff(roll_t)));
% Fit transfer function (2nd-order)
roll_sys = tfest(roll_data_iddata, 2);

```

Listing 4.12: Roll Transfer Function Estimation

The estimated transfer function `roll_sys` is then converted to a state-space representation (`roll_ss_sys`) to facilitate LQR design.

State-Space Matrix Extraction and Controllability Check After obtaining the transfer function, it is converted into a state-space representation. This form provides the system matrices (A, B, C, D) which are essential for designing state-feedback controllers

like LQR. The controllability is than checked by examining the rank of the controllability matrix.

```

1 % Convert to state-space
2 roll_ss_sys = ss(roll_sys);
3 roll_A = roll_ss_sys.A;
4 roll_B = roll_ss_sys.B;
5 roll_C = roll_ss_sys.C;
6 roll_D = roll_ss_sys.D;
7 % Check controllability
8 if rank ctrb(roll_A, roll_B) == size(roll_A, 1)
9     disp('Roll System is controllable');
10 else
11     error('Roll System is uncontrollable! Check model.');
12 end

```

Listing 4.13: Roll State-Space Extraction and Controllability Check

4.3. Controller Design

After system identification was performed, a controller can be designed for the specific system. The controller design was paramount to this research; a high emphasis was placed on system performance, and proper controller design would directly drive this. As a result, a large amount of effort was put into both the design and tuning of the controller.

4.3.1. Original PID Controller

The system originally utilized a very basic PID controller. Tuning was conducted with the Ziegler-Nichols method, and the following gains were found for each subsystem:

Table 4.4.: Ziegler-Nichols PID Gains for Roll and Pitch Subsystems

Subsystem	k_p	k_i	k_d
Roll	35	50	5
Pitch	60	110	5

However, with these values, when full PID control was used, the system would rapidly vibrate, leading to uncontrolled system behavior and unacceptable noise and vibration. Because of this, the original system was only ever used with PD control, and its performance suffered greatly. Following sinusoidal trajectories, it would frequently undershoot or overshoot the setpoint and responded poorly to perturbations. As a result, an improved controller method needed to be developed.

4.3.2. MPC

During the initial ideation of the control algorithm several possible control schemes were examined. One of these was model predictive control (MPC). MPC uses a dynamic model of the system to predict system behavior and determine a control input based on the model dynamics[23]. While this control technique is extremely high performance it implementation was limited by both a limited model that only accounted for the mass and inertia properties and the high computational power to simultaneously run and predict the model's behavior. This system utilized low-cost hardware with limited computational resources and, as a result, lacked the computational power to perform MPC.

4.3.3. Gain Scheduling and Adaptive Control

It was clear that due to varying system dynamics across the system's range of motion, adaptive control or gain scheduling would be a very valuable asset for improving system performance. Adaptive control estimates unknown or time-varying system parameters based on real-time performance feedback [24]. In contrast, gain scheduling is a pre-programmed approach where controller parameters are driven by preprogrammed and scheduled gains[25].

With relatively little additional computational power and complexity, the control gains could be calculated and interpolated based on the system's position, making gain scheduling an excellent candidate for improving system performance.

After the previously discussed multi-point system identification, a set of gains was calculated for each characterization point. These gains were then stored in tables, and the controller would interpolate between these gains based on the current position of the system using the following code.

```

// === Linear interpolation between two values ===
double interpolate(double x, double x0, double x1, double y0, double y1) {
    return y0 + (y1 - y0) * ((x - x0) / (x1 - x0));
}

```

Listing 4.14: Linear Interpolation for Gain Scheduling

The gains used for the roll and pitch subsystems are presented in Table 4.5, Table 4.6, Table 4.7, Table 4.8, and Table 4.9. These gains were calculated based on the system identification results and were tuned to achieve optimal performance at each characterization point. The specific calculation of these gains was done in Matlab at each point using the following procedure:

For the roll axis, once the state-space matrices were identified at each point, the weighting matrices Q and R were defined:

```

% LQR weight matrices
Q = diag([500, 0.25]); % Penalize position error more than velocity
R = 0.0075; % Penalize control effort

```

Listing 4.15: Weighting Matrix definition

The pitch axis used a very similar procedure; however, the Q matrix was augmented with the Integral penalty component Qi:

```

% LQI weight matrices
Q = diag([500, 0.25, 0.01]); % Penalize position error more than velocity

```

Listing 4.16: LQI Weighting Matrix definition

Then, the LQR gains at each point could be calculated using the ‘lqr’ Matlab command:

```

% Compute LQR gain
[K, S, CLP] = lqr(A, B, Q, R);

```

Listing 4.17: LQR and LQI Gain Calculation

This was done for each characterization point in the system for both pitch and roll and resulted in the following gains:

Table 4.5.: Roll Proportional Gain (K_p) Table

Pitch \ Roll	-15	0	15
-20	135.41	135.41	137.91
0	136.23	132.23	130.12
20	137.36	135.77	131.78

Table 4.6.: Roll Derivative Gain (K_d) Table

Pitch \ Roll	-15	0	15
-20	0.6527	1.0829	0.43766
0	0.6854	0.7588	0.4810
20	0.6579	1.0788	0.42543

Table 4.7.: Pitch Proportional Gain (K_p) Table

Pitch \ Roll	-15	0	15
-20	188.07	195.37	191.11
0	161.41	166.32	167.01
20	153.37	155.56	151.23

Table 4.8.: Pitch Derivative Gain (K_d) Table

Pitch \ Roll	-15	0	15
-20	0.3124	0.3256	0.3154
0	0.3671	0.3671	0.3272
20	0.3643	0.3374	0.3576

Table 4.9.: Pitch Integral Gain (K_i) Table

Pitch \ Roll	-15	0	15
-20	0.143744	0.185649	0.164665
0	0.135649	0.153566	0.155123
20	0.124432	0.155649	0.134566

4.3.4. LQR and LQI Control

Linear Quadratic Regulator (LQR) control and Linear Quadratic Integral (LQI) control are cost-optimal control algorithms that minimize a quadratic cost function. LQI control builds upon the efforts of LQR control by incorporating integral action in an effort to reduce steady state error.

Both of these control methods are well-suited to this research as they achieve a good balance of high system performance with minimal control efforts. LQR control was chosen for the roll joint, and LQI control was chosen for the pitch joint in an effort to minimize steady state error.

The objective of LQR control is to find a control input $\mathbf{u}(t)$ that minimizes the following quadratic cost function:

$$J_{LQR} = \int_0^{\infty} (\mathbf{x}^T(t) Q \mathbf{x}(t) + \mathbf{u}^T(t) R \mathbf{u}(t)) dt$$

where:

- $\mathbf{x}(t)$ is the state vector.
- $\mathbf{u}(t)$ is the control input vector.
- Q is a weighting matrix for the states, penalizing deviations from the desired state
- R is a weighting matrix for the control inputs, penalizing control effort.

For LQI control, the integral of the error is added to the system, and the cost function is also minimized. If $\mathbf{e}_I(t)$ represents the integral of the output error, the augmented state $\mathbf{x}_{aug}(t)$ includes the original states and the integral error. The cost function for LQI is

then:

$$J_{LQI} = \int_0^{\infty} (\mathbf{x}_{aug}^T(t) \tilde{Q} \mathbf{x}_{aug}(t) + \mathbf{u}^T(t) R \mathbf{u}(t)) dt$$

where \tilde{Q} is the augmented weighting matrix for the states, including a penalty on the integral error to drive it to zero.

The specific Q and R matrices used for this controller were numerically determined by trial and error during the research to maximize system while maintaining stability.

The following is a detailed implementation of the LQR and LQI controllers in the PSM software.

Roll LQR Controller Implementation

The calculated LQR gains were input as a vector to the LQR control function along with the commanded position and the actual position. From here several key variables were initialized. The current time was determined and from this the Δt value was calculated then used to calculate the actual velocity. A low-pass filter was then applied to this value. The velocity and positional error were then determined and the control input was calculated from these error values scaled by their respective gains K_p and K_d . The implementation of this in the system software can be seen below.

```

float compute_roll_LQR_control(float gains, float commanded_position, float
actual_position) {
    static float previous_position_roll = 0.0f;
3     static unsigned long previous_time_roll = 0;
    static float filtered_velocity_roll = 0.0f;
    const float alpha = 0.9f;

    unsigned long current_time = micros();
8     float delta_time = (current_time - previous_time_roll) / 1000000.0f;
    if (delta_time <= 0.0f) delta_time = 0.000001f;

    float raw_velocity = (actual_position - previous_position_roll) /
        delta_time;
    filtered_velocity_roll = alpha * filtered_velocity_roll + (1.0f - alpha) *
        raw_velocity;
13
    previous_position_roll = actual_position;
    previous_time_roll = current_time;

    float position_error = commanded_position - actual_position;
18     float state[2] = {position_error, filtered_velocity_roll};

    float control_input = 0.0f;
    for (int i = 0; i < 2; i++) {
        control_input -= gains[i] * state[i];
23     }

    return control_input;
}

```

Listing 4.18: Roll LQR Control Input Calculation

Pitch LQI Controller Implementation (with Feedforward)

The Pitch joint LQI controller implementation was very similar to the Roll joint LQR controller implementation. The function input a gain vector along with actual position and commanded positions. These values were then used to calculate the positional and velocity error values. The positional error was then multiplied by Δt to calculate the integral error. These errors were scaled by their respective gain values and the control input before feedforward control was calculated. To calculate the feedforward control

input component, the B^\dagger matrix is multiplied by the sum of the system's A matrix and the reference state. The U_{ff} is then scaled by λ and added to the original control input. The detailed software implementation can be seen below:

```

float compute_pitch_LQI_control(float gains, float commanded_position, float
actual_position) {
    static float previous_position_pitch = 0.0f;
    static float previous_commanded_position_pitch = 0.0f;
4   static unsigned long previous_time_pitch = 0;
    static float integral_error = 0.0f;
    const float lambda = 0.0f;

    const float A[2][2] = {{-4.3950, -2.3842}, {4.0000, 0.0}};
9   const float B_dagger[2][2] = {{0.5, 0.0}, {0.0, 0.0}};

    unsigned long current_time = micros();
    float delta_time = (current_time - previous_time_pitch) / 1000000.0f;
    if (delta_time <= 0.0f) delta_time = 0.000001f;
14

    float raw_velocity = (actual_position - previous_position_pitch) /
        delta_time;
    previous_position_pitch = actual_position;
    previous_time_pitch = current_time;

19   float position_error = commanded_position - actual_position;
    integral_error += position_error * delta_time;

    float state[3] = {position_error, raw_velocity, integral_error};

24   float control_input = 0.0f;
    for (int i = 0; i < 3; i++) {
        control_input -= gains[i] * state[i];
    }

29   float x_ref_dot = (commanded_position - previous_commanded_position_pitch)
        / delta_time;
    previous_commanded_position_pitch = commanded_position;

    float x_ref[2] = {commanded_position, x_ref_dot};
    float u_ff = 0.0f;
34   for (int i = 0; i < 2; i++) {
        float Ax_ref = 0.0f;
        for (int j = 0; j < 2; j++) {
            Ax_ref += A[i][j] * x_ref[j];
        }
        u_ff += B_dagger[i][i] * (Ax_ref + x_ref_dot);
    }

39   control_input += lambda * u_ff;
}

44   return control_input;
}

```

50

Listing 4.19: Pitch LQI Control with Feedforward

4.3.5. Feedforward Control

Feedforward control is a control method which attempts to anticipate changes or disturbances to the system's input. It was theorized that a feedforward control strategy could further reduce any remaining steady-state error in the pitch subsystem.

In order for feedforward control to be implemented, a model of the system must be constructed in the form of a specific matrix known as the B^\dagger matrix. The B^\dagger matrix is formulated through the Moore-Penrose pseudoinverse. It is formulated as follows:

Let B be an $m \times n$ real or complex matrix. Its Singular Value Decomposition (SVD) is given by:

$$B = U\Sigma V^T$$

where:

- U is an $m \times m$ unitary (or orthogonal for real matrices) matrix whose columns are the left singular vectors of B .
- Σ is an $m \times n$ rectangular diagonal matrix with non-negative real numbers on the diagonal, called the singular values of B , typically arranged in decreasing order.
- V^T is an $n \times n$ unitary (or orthogonal for real matrices) matrix whose rows are the right singular vectors of B . (V is the matrix of right singular vectors).

The **Moore-Penrose pseudoinverse** of B , denoted B^\dagger , is then defined as:

$$B^\dagger = V\Sigma^\dagger U^T$$

where Σ^\dagger is an $n \times m$ matrix formed by taking the reciprocal of each non-zero singular value on the diagonal of Σ , and then transposing the matrix.

For the purpose of this research, this matrix could be calculated via the MATLAB command `pinv`. This command, when applied to the identified B matrix from the system identification procedure, would result in the B^\dagger matrix.

This procedure was conducted for each of the characterization points previously discussed. Upon calculation of the B^\dagger matrix, this matrix is used to calculate u_{ff} by multiplying the B^\dagger matrix (pseudoinverse of the input matrix) with the sum of the system's A matrix multiplied by the reference state and the time derivative of the reference state. This u_{ff} is then scaled by a factor λ , which can be tuned from 0 to 1.0 to adjust the feedforward element of the controller.

The ultimate result of this control effort is to proactively cancel anticipated system dynamics and generate better system performance.

4.3.6. Comprehensive Control Strategy

The final controller for the system was a resulting combination of several of the control strategies previously discussed. Ultimately, for the roll joint, it was found that gain scheduling with an LQR controller provided adequate system performance. However, for the pitch subsystem, this method needed to be improved upon due to consistent steady-state error in the form of target undershooting. To remedy this, an LQI controller with feedforward implementation and gain scheduling was employed. These strategies led to drastic improvements in system performance.

5. System evaluation

In order assess effectiveness of the controller design, a testing procedure was developed. This procedure and its associated results will be explored in this section.

5.1. Overview of Experiments

The performance of the control system was assessed through two types of experiments. These were designed to assess performance under various trajectory conditions.

- **Sinusoidal Path Following:** In this experiment, the commanded trajectory consisted of a pregenerated sinusoidal path which the system was required to follow. The path was designed such that it would test the system's performance in tracking a smooth, continuous trajectory while also maintaining stability. The period of the sin wave was chosen to highlight rapid changes in desired trajectory velocities that the system might experience. Its amplitude was selected to push the system towards its positional limits in each axis. For the pitch axis a period of 3 seconds with an amplitude of ± 15 degrees was chosen whereas for the roll axis a period of 3 seconds and an amplitude of ± 20 degrees was chosen.
- **Target Following:** In this experiment the PSM followed real clinical trajectories generated by the MTM in simulated surgical procedures. The MTM was used to generate a path that both axes then attempted to follow. The exact 3D trajectory followed during this experiment can be seen in Figure 5.1.

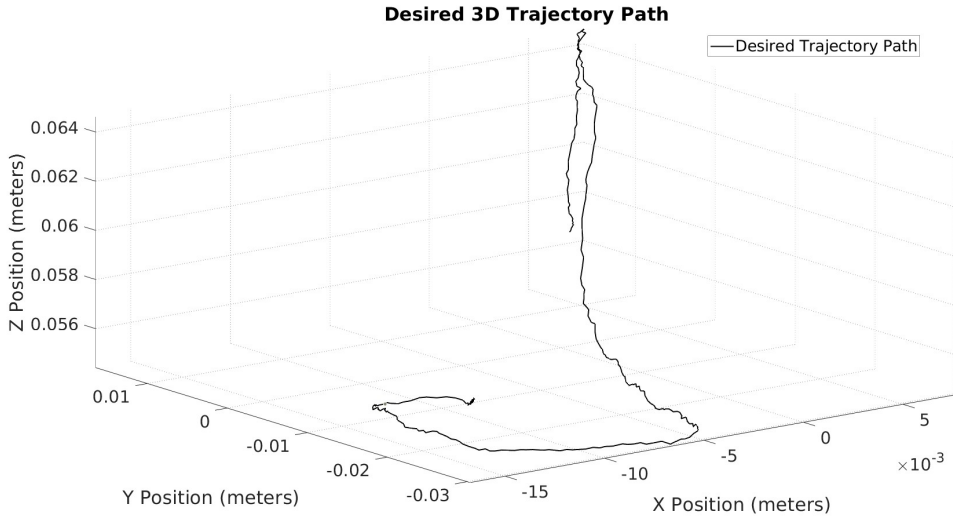


Figure 5.1.: The 3D trajectory generated by the MTM, representing a typical surgical movement for target following experiments.

The newly developed control scheme was tested alongside the previously used controller. During each experimental trial, the target position, actual positions, commanded motor speed, and positional error were tracked, logged and then parsed and plotted by a custom MATLAB script. The following sections detail the results of these experiments, focusing on positional error performance.

5.2. Control Algorithm Performance

These experiments revealed a significant increase in performance for the new control algorithm. During both the sinusoidal path following and trajectory following experiments, the positional error was reduced in both the roll and pitch axes.

5.2.1. Sinusoidal Path Following Experiment Results

With the previous proportional control algorithm, the system consistently undershot the target position and lagged behind the intended trajectory, particularly at the extrema of the joint angles. This is highlighted in Figure 5.2 and Figure 5.3, which show the system's performance during sinusoidal path following with proportional control.

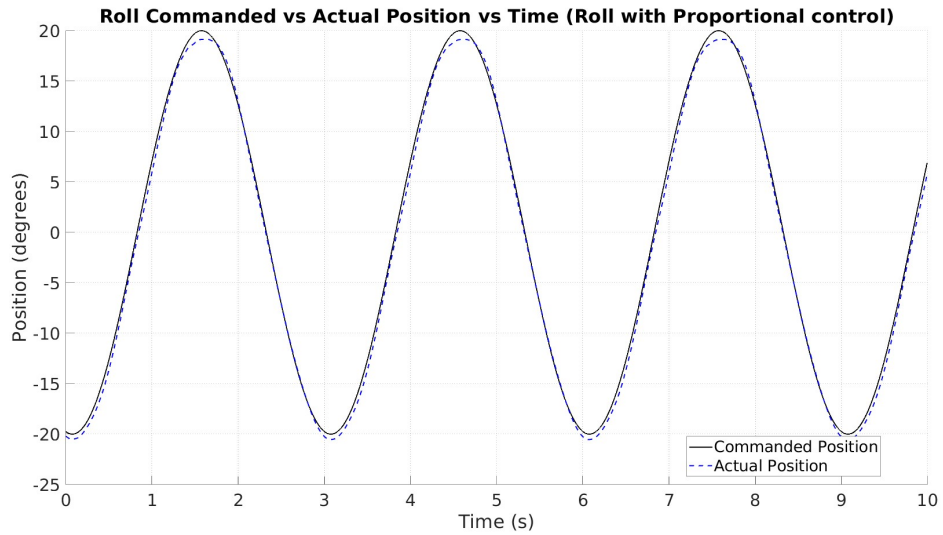


Figure 5.2.: Sinusoidal path following performance of the Roll axis with proportional control, showing significant lag and overshoot.

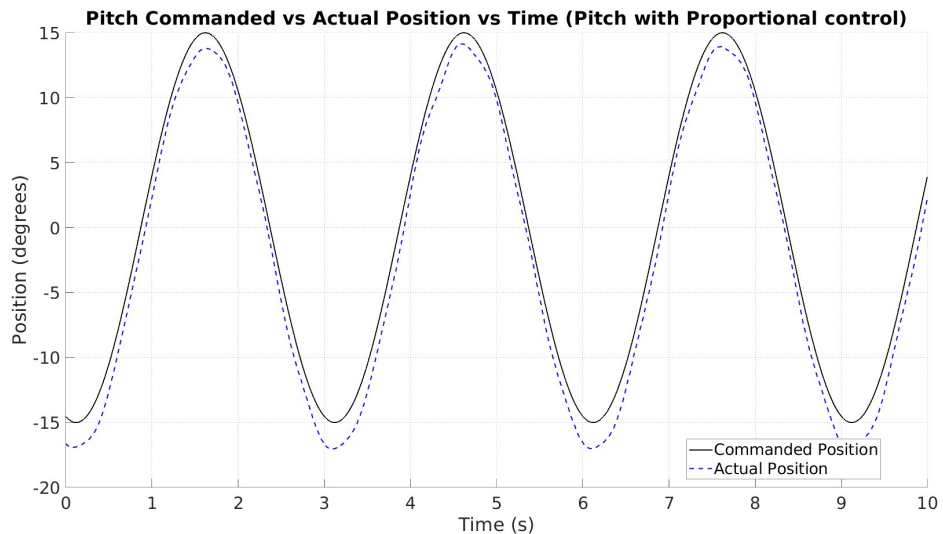


Figure 5.3.: Sinusoidal path following performance of the Pitch axis with proportional control, illustrating substantial undershoot and lag.

The performance of the new control algorithm for sinusoidal path following was excellent. The system consistently followed the sinusoidal path with little to no lag, undershoot, or overshoot. This can clearly be seen in Figure 5.4 and Figure 5.5, where there

is almost no noticeable difference between the commanded position and the actual position.

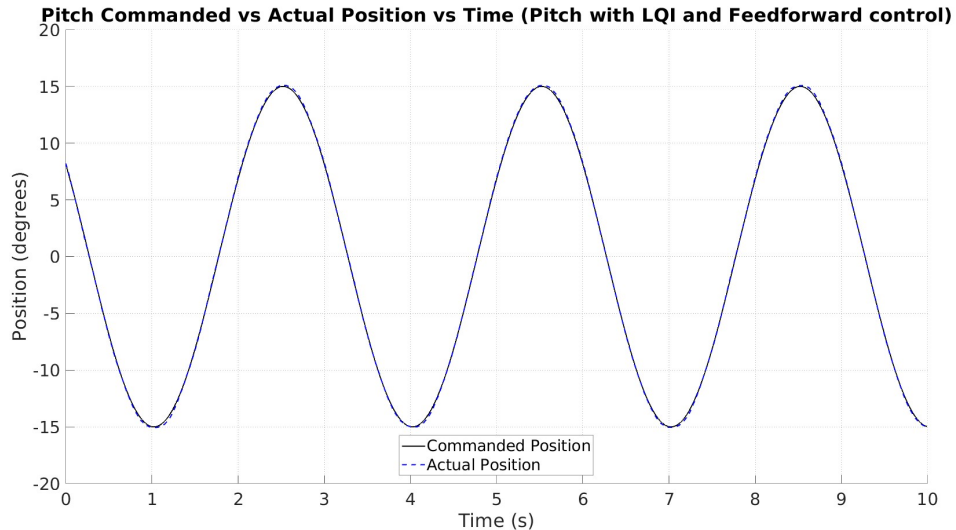


Figure 5.4.: Sinusoidal path following performance of the Pitch axis with the new LQI control algorithm, demonstrating excellent tracking with minimal error.

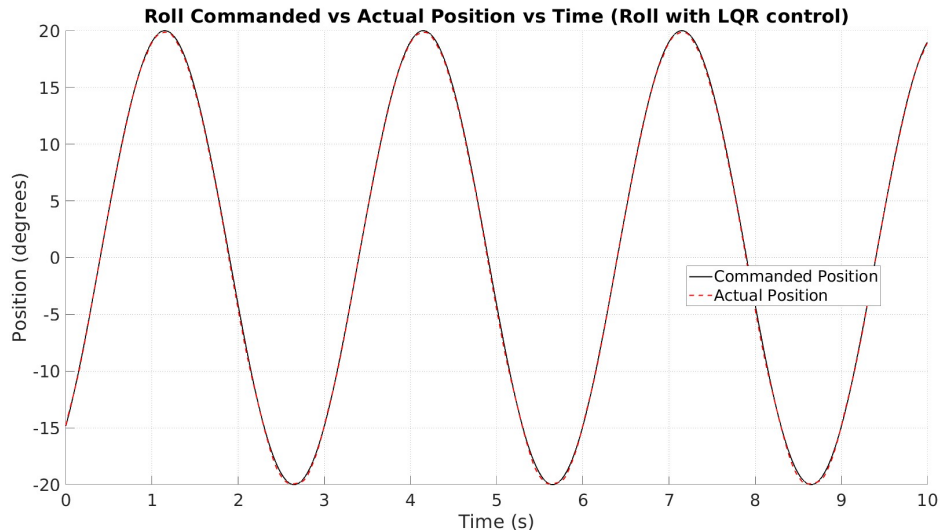


Figure 5.5.: Sinusoidal path following performance of the Roll axis with the new LQR control algorithm, showing near-perfect tracking.

With the proportional control algorithm, the error in the pitch axis reached a maximum value of 2.31° , while the error in the roll axis reached 1.17° . The overall average error for the pitch axis was 1.52° , and the overall average error for the roll axis was 0.62° . These errors were particularly pronounced at the extrema of the joint angles, where the system struggled to maintain accuracy and stability.

With the new control algorithms, the maximum error in the pitch axis was reduced to 0.35° , and the maximum error in the roll axis was reduced to 0.41° . Both of these errors occurred at the extreme limits of their respective axes, and the average error of the pitch axis over the trial was 0.12° , while the value for the average error over the trial for the roll DOF was 0.21° .

The comparison of these errors between the control methods through the sinusoidal path following procedure can be seen in Figure 5.6 and Figure 5.7, where it is clear that the error for the new control method is much smaller than the older control method.

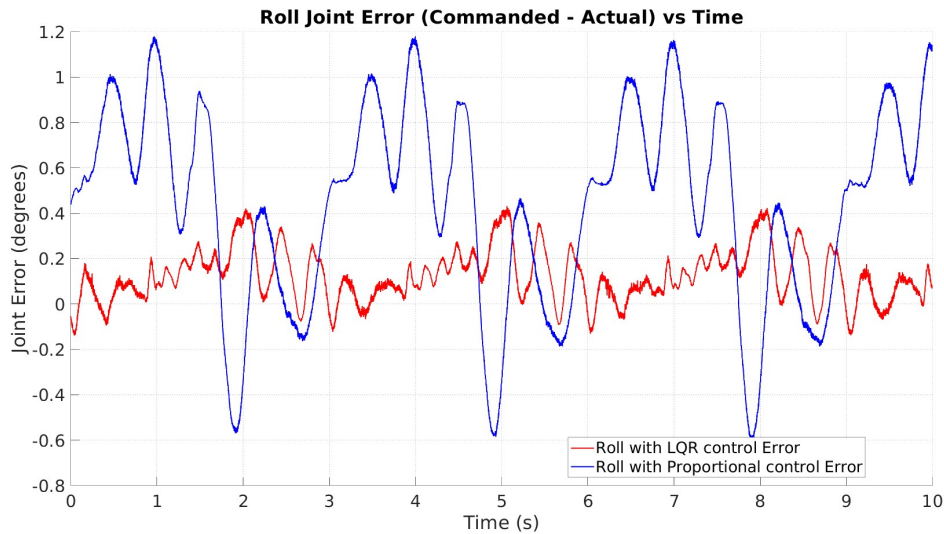


Figure 5.6.: Comparison of Roll axis tracking error for proportional control vs. the new LQR control during sinusoidal path following.

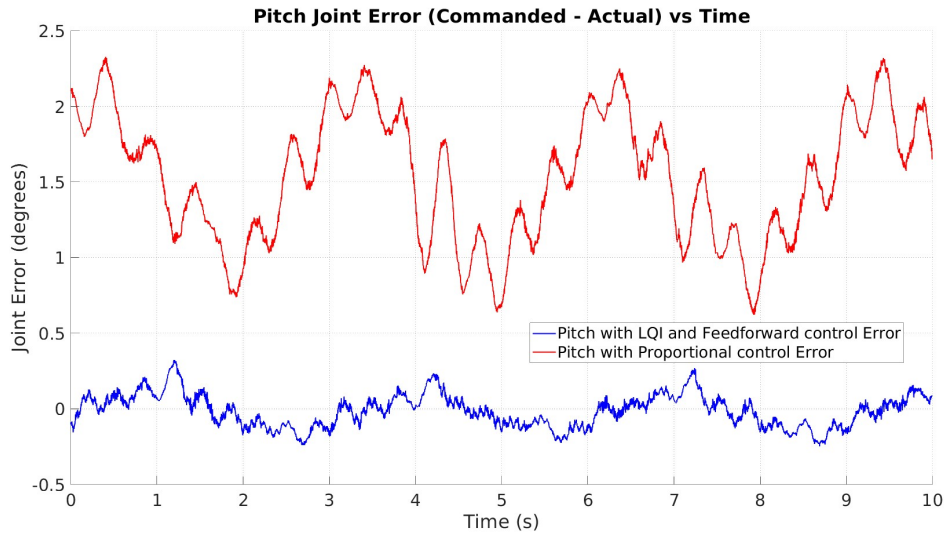


Figure 5.7.: Comparison of Pitch axis tracking error for proportional control vs. the new LQI control during sinusoidal path following.

During sinusoidal path following, the new control algorithm's performance far exceeded that of the previous design. However, this procedure is not fully representative of real-world scenarios. During actual surgical procedures, the desired trajectory will very rarely be such a smooth, predictable path. As a result of this shortcoming, the system's performance following a real trajectory path must be examined.

5.2.2. Target Following Experiment

Similarly to the sinusoidal path following experiment, the new control algorithm's performance in the target path following experiment far exceeded that of the older control algorithm. This experiment used the 3D trajectory path shown in Figure 5.1, which is representative of typical surgical movements.

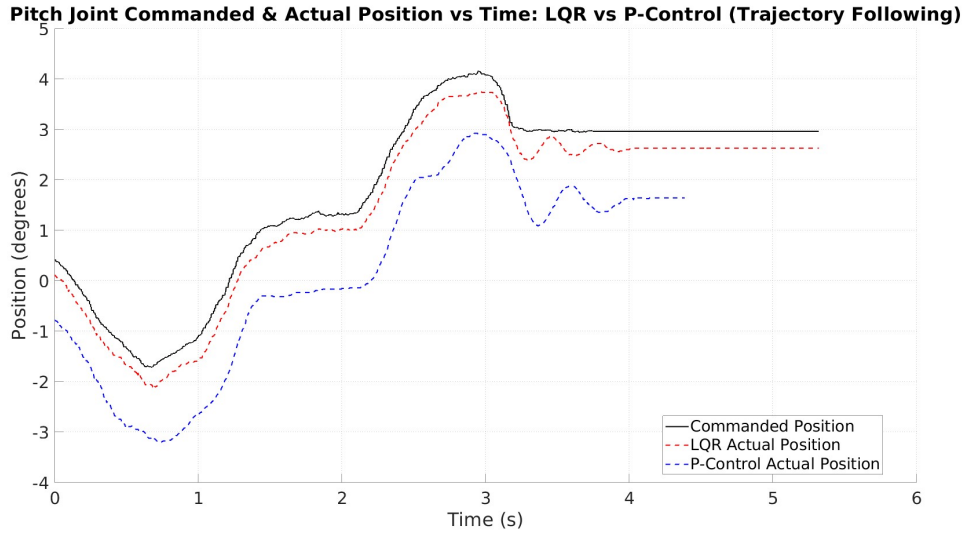


Figure 5.8.: Target path following performance of the Pitch axis, comparing the old proportional control to the new LQR control algorithm. The new controller exhibits significantly improved tracking accuracy.

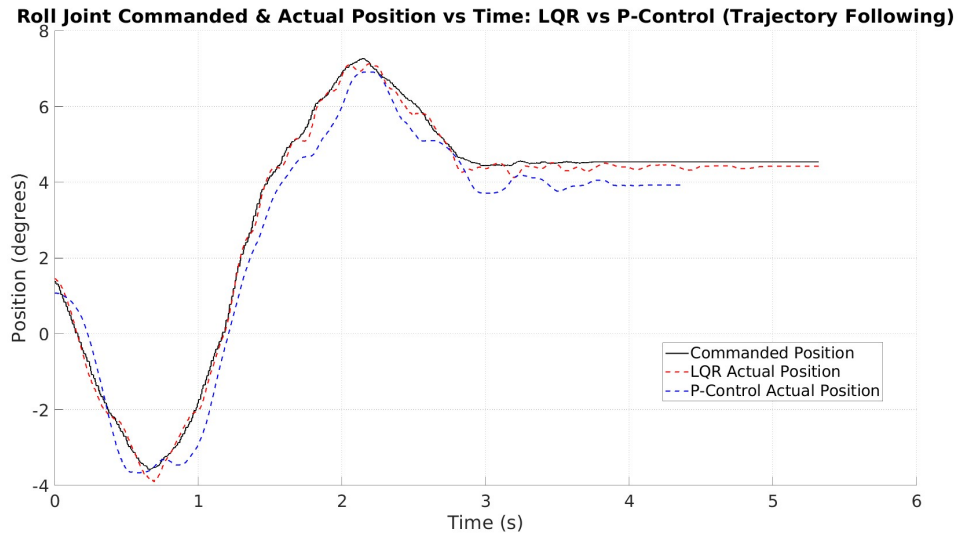


Figure 5.9.: Target path following performance of the Roll axis, comparing the old proportional control to the new LQR control algorithm.

The reduction in error is clearly evident when comparing the old and new control methods. With the new LQR and LQI with feedforward control, the system maintained a much tighter adherence to the desired trajectory. This is visually represented in the er-

rror plots in Figure 5.10 and Figure 5.11, which show a substantial decrease in tracking error compared to the previous proportional control.

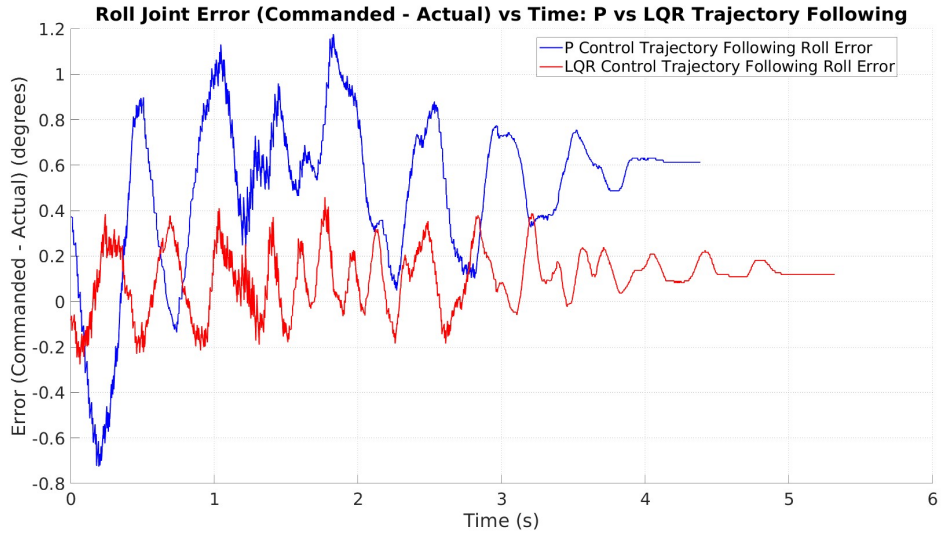


Figure 5.10.: Comparison of Roll axis tracking error for proportional control vs. the new LQR control during complex target path following.

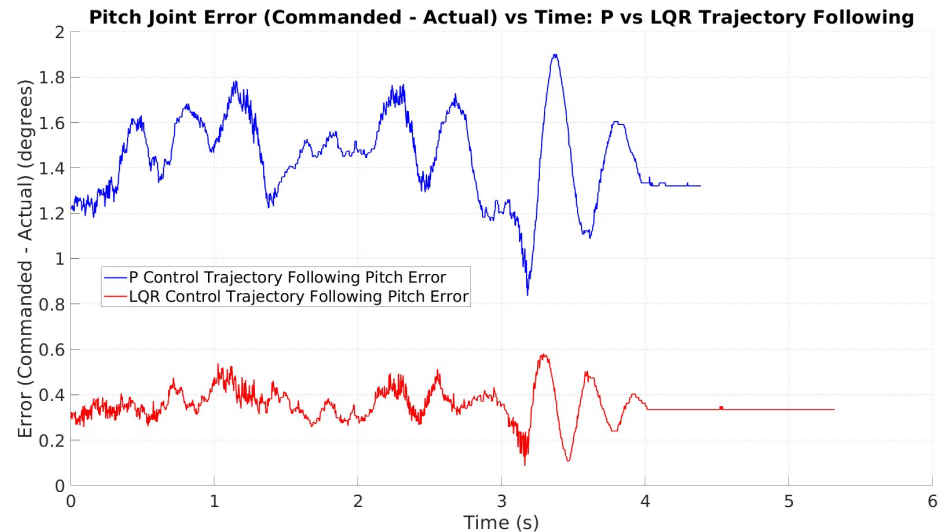


Figure 5.11.: Comparison of Pitch axis tracking error for proportional control vs. the new LQR control during complex target path following.

6. Conclusion and Future Work

The research aims of this project were successfully achieved. The system software architecture was updated from an Arduino C-based implementation to a more modern ROS 2 software framework. Additionally, the overall system performance was drastically improved through more robust system identification and control methods.

6.1. Key Findings

Updating the software framework provided few quantitative performance improvements; however, qualitatively, the system framework is now more scalable. The SDF model allows for future work in collision detection, and the node-based architecture of the ROS 2 system created a robust platform for future development.

The improved system identification and control methods provided clear performance gains. Both the maximum and average positional error seen by the system were drastically reduced in all trials, and the system achieved smooth and stable performance during trajectory tracking.

6.2. Limitations

Throughout this research, significant hardware limitations became apparent. The original system was designed for ease of manufacturing and assembly, which led to many components being 3D printed. While this method was a simple and low-cost way to create the complex geometries required, the low stiffness of the plastic parts resulted in poor system performance.

During movement, the end-effector tip could be seen oscillating, a behavior that would be unacceptable in clinical procedures. Furthermore, prolonged use revealed that the

components exhibited plastic creep. Many linkages warped beyond their specified tolerances, causing binding within the system and, in some instances, overcoming press-fits and disassembling during operation. Finally, the capstan cable tension proved inconsistent, frequently loosening and rendering previous system identifications obsolete.

Additionally the ROS 2 implementation is limited to core middleware functionalities, and some advanced features such as security enhancements are not fully explored. Finally due to resource constraints, long-term reliability and robustness tests were not conducted. These limitations highlight potential areas for future research to extend the applicability and performance of the system.

6.3. Recommendations for Future Work

Before further research is conducted, it is recommended that the system's hardware be improved. The superstructure of the joints should be redesigned for increased stiffness, and more robust assembly methods must be employed. Additionally, a more consistent tensioning method for the capstan drives should be implemented, or the reduction technique must be changed altogether.

6.4. Final Remarks

Despite its hardware shortcomings, the objectives of this research were achieved. The system's software architecture was updated to a modern ROS 2 standard, and its performance was greatly improved through more robust identification and control techniques. While the system still requires improvements before it can replicate clinical procedures, the research conducted in this paper lays the groundwork for future development.

Bibliography

- [1] A. R. Lanfranco, A. E. Castellanos, J. P. Desai, and W. C. Meyers, "Robotic surgery: a current perspective," *Annals of Surgery*, vol. 239, no. 1, pp. 14–20, 2004.
- [2] Johns Hopkins University and Intuitive Surgical, "The da Vinci Research Kit (dVRK) Components," https://research.intusurg.com/index.php/Main_Page, 2025, accessed: July 14, 2025.
- [3] Johns Hopkins University and Worcester Polytechnic Institute and Intuitive Surgical. (2025) The da Vinci Research Kit (dVRK) Documentation. Accessed: July 14, 2025. [Online]. Available: <https://dvrk.readthedocs.io/main/index.html>
- [4] B. Hannaford, J. Rosen, D. W. Friedman, H. King, P. Roan, L. Cheng, D. Gozman, J. Ma, S. N. Kosari, and L. White, "Raven-ii: An open platform for surgical robotics research," *IEEE Transactions on Biomedical Engineering*, vol. 60, no. 4, pp. 954–959, 2013.
- [5] G. A. Fontanelli, F. Ficuciello, L. Villani, and B. Siciliano, "Modelling and identification of the da vinci research kit robotic arms," *2017 IEEE/RSJ International Conference on Intelligent Robots and Systems (IROS)*, pp. 1464–1469, 2017. [Online]. Available: <https://api.semanticscholar.org/CorpusID:1928260>
- [6] B. Hannaford, J. Rosen, D. W. Friedman, H. King, M. Sinanan, and R. Satava, "Raven-ii: An open platform for surgical robotics research," *IEEE Transactions on Biomedical Engineering*, vol. 60, no. 4, pp. 954–959, 2013.
- [7] RobotsGuide.com. (2024) Raven Surgical Robot. [Online]. Available: <https://robotsguide.com/robots/ravensurgical/>
- [8] Z. Chen, A. Deguet, R. Taylor, S. Dimaio, G. Fischer, and P. Kazanzides, "An open-source hardware and software platform for telesurgical robotics research," *The MIDAS Journal*, 08 2013.

- [9] S. Macenski, T. Foote, B. Gerkey, C. Lalancette, and W. Woodall, “Robot operating system 2: Design, architecture, and uses in the wild,” *Science Robotics*, vol. 7, no. 66, p. eabm6074, 2022. [Online]. Available: <https://www.science.org/doi/abs/10.1126/scirobotics.abm6074>
- [10] P. Kazanzides, P. Oppenheimer, X. Chai, J. Lee, R. Khakha, F. Chen, R. H. Taylor, G. H. F. Johnson, K. Y. Chiu, Y. Lee, R. N. H. Taylor, R. H. S. Taylor, and T. Maros, “The da Vinci Research Kit: A Platform for Open Surgical Robotics Research,” in *2014 IEEE/RSJ International Conference on Intelligent Robots and Systems (IROS)*, 2014, pp. 2455–2461.
- [11] A. M. Okamura, F. Simone, and M. D. O’Leary, “Force feedback for robotic surgery,” *IEEE Engineering in Medicine and Biology Magazine*, vol. 20, no. 3, pp. 26–30, 2001.
- [12] R. Maier, F. Schick, D. Heger, C. D. Klink, M. Gessat, J. Roth, J. Schipper, J. Weiler, F. Nickel, and R. Dillmann, “The role of image guidance for robotic-assisted surgery – A review,” *International Journal of Computer Assisted Radiology and Surgery*, vol. 10, no. 10, pp. 1587–1604, 2015.
- [13] H. Wang, Z. Li, L. Xu, L. Zhang, J. Zhang, Y. Zheng, and G. Yan, “Deep Learning for Real-time Tissue Classification in Robotic Surgery,” *IEEE Transactions on Medical Imaging*, vol. 39, no. 6, pp. 2174–2184, 2020.
- [14] X.-G. Xia, “System Identification Using Chirp Signals and Time-Variant Filters in the Joint Time-Frequency Domain,” *IEEE Transactions on Signal Processing*, vol. 45, no. 8, pp. 2072–2084, aug 1997.
- [15] A. B. Martinsen, A. M. Lekkas, and S. Gros, “Combining system identification with reinforcement learning-based mpc,” *IFAC-PapersOnLine*, vol. 53, no. 2, pp. 8130–8135, 2020, 21st IFAC World Congress. [Online]. Available: <https://www.sciencedirect.com/science/article/pii/S2405896320329542>
- [16] T. Oddos, G. Stamatias, C. Coret, J. Hourihane, and A. D. Irvine, “Robotic surgical system with improved control based on actuator characterization,” Patent US20230309921A1, 2023. [Online]. Available: <https://patents.google.com/patent/US20230309921A1>
- [17] A. Walder, “Design and validation of a teleoperated surgical training system,” Master of Science in Engineering, Management Center Innsbruck, Innsbruck, 2022, student ID: 2010869015.

- [18] M. Preiss, A. Walder, and Y. Kim, "Haptically enhanced vr surgical training system," *Current Directions in Biomedical Engineering*, vol. 8, no. 2, pp. 737–740, 2022.
- [19] M. Messner, "Design and development of a scaled-down teleoperative surgical robotic system for training applications," 2025.
- [20] ROS Wiki and S. Brawner, "SolidWorks to URDF Exporter," https://wiki.ros.org/sw_urdf_exporter, accessed: 2025-07-18.
- [21] BruceChanJianLe, "ign-gz-urdf-to-sdf," <https://github.com/BruceChanJianLe/ign-gz-urdf-to-sdf>, accessed: 2025-07-18.
- [22] L. I. U. Bo, Z. H. A. O. Jun, and Q. I. A. N. Jixin, "Design and analysis of test signals for system identification," in *Computational Science – ICCS 2006*, V. N. Alexandrov, G. D. van Albada, P. M. A. Sloot, and J. Dongarra, Eds. Berlin, Heidelberg: Springer Berlin Heidelberg, 2006, pp. 593–600.
- [23] K. S. Holkar and L. M. Waghmare, "An overview of model predictive control," *International Journal of control and automation*, vol. 3, no. 4, pp. 47–63, 2010.
- [24] K. J. Åström, *Adaptive Control*. Berlin, Heidelberg: Springer Berlin Heidelberg, 1991, pp. 437–450. [Online]. Available: https://doi.org/10.1007/978-3-662-08546-2_24
- [25] V. Fromion and G. Scorletti, "A theoretical framework for gain scheduling," *International Journal of Robust and Nonlinear Control*, vol. 13, no. 10, pp. 951–982, 2003. [Online]. Available: <https://onlinelibrary.wiley.com/doi/abs/10.1002/rnc.748>

List of Figures

2.1. The Original Da Vinci Research Kit.(Reprinted from [5] Fig 1)	5
2.2. The Raven II surgical system design. In this figure the cable driven de-sign can clearly be seen (Reprinted from [6] Fig 1)	6
2.3. An overview of a typical ROS 2 node network consisting of subscription nodes and publishing nodes, actions and service types can also be seen (Reprinted from [9] Fig 2)	7
3.1. Overview of the Desktop Teleoperated Surgical Training System, illustrating the MTM and PSM components.	10
3.2. Overview of the MTM with indicated DOFs.	11
3.3. Overview of the PSM with indicated DOFs.	12
3.4. Detailed view of the MTM's J1 joint design (Reprinted from [17] Fig 2.1) .	14
3.5. Detailed overview of the MTM's GCS design. (Reprinted from [17] Fig 2.9)	15
3.6. Detailed view of the mechanical design of the roll axis, highlighting the main shaft design. (Reprinted from [17] Fig 2.10)	17
3.7. A detailed view of the PSM's pitch and roll GCS design. (Reprinted from [17] Fig. 2.22)	18
3.8. Detailed view of the PSM's pitch axis mechanism. (Reprinted from [17] Fig 2.13)	19
3.9. Detailed view of the PSM's insertion axis mechanism. (Reprinted from [17] Fig 2.14)	20
3.10. Detailed view of the PSM's tool cart, highlighting the spring-loaded com-pliance mechanism. (Reprinted from [17] Fig 2.15)	21
3.11. The MTM and its associated degrees of freedom shown in their zero-position with DH-coordinate frames attached (Reprinted from [17] Fig 3.1)	24
3.12. The updated gimbal and its associated degrees of freedom shown in their zero-position. (Reprinted from [19] Fig 2.1)	24

3.13.The PSM and endowrist tool shown in their zero-position with DH-coordinate frames attached, according to the cDH convention. (Reprinted from [17] Fig 3.2)	25
4.1. Initial ROS 2 System Architecture for Target Pose Calculation.	26
4.2. Simplified ROS 2 System Architecture for Direct Target Pose Streaming.	27
4.3. SDF model of MTM shown in the RViz environment. The gimbal solid models have been hidden in this model	28
4.4. Theoretical trend of absolute motor voltage required for the roll subsystem as a function of roll angle.	38
4.5. Theoretical trend of required motor voltage for the pitch subsystem as a function of pitch angle.	38
5.1. The 3D trajectory generated by the MTM, representing a typical surgical movement for target following experiments.	54
5.2. Sinusoidal path following performance of the Roll axis with proportional control, showing significant lag and overshoot.	55
5.3. Sinusoidal path following performance of the Pitch axis with proportional control, illustrating substantial undershoot and lag.	55
5.4. Sinusoidal path following performance of the Pitch axis with the new LQI control algorithm, demonstrating excellent tracking with minimal error.	56
5.5. Sinusoidal path following performance of the Roll axis with the new LQR control algorithm, showing near-perfect tracking.	56
5.6. Comparison of Roll axis tracking error for proportional control vs. the new LQR control during sinusoidal path following.	57
5.7. Comparison of Pitch axis tracking error for proportional control vs. the new LQI control during sinusoidal path following.	58
5.8. Target path following performance of the Pitch axis, comparing the old proportional control to the new LQI control algorithm. The new controller exhibits significantly improved tracking accuracy.	59
5.9. Target path following performance of the Roll axis, comparing the old proportional control to the new LQR control algorithm.	59
5.10. Comparison of Roll axis tracking error for proportional control vs. the new LQR control during complex target path following.	60
5.11. Comparison of Pitch axis tracking error for proportional control vs. the new LQI control during complex target path following.	60

List of Tables

3.1. MTM Joint Classification and Positional Sensing.	10
3.2. PSM Joint Classification and Drive System.	11
3.3. PSM Joint Specifications	21
3.4. Initial PID Constants	23
4.1. MTM ROS2 Topics	30
4.2. Overview of Primary Files in the PSM Software Codebase	34
4.3. Grid of 9 Characterization Points for System Identification	39
4.4. Ziegler-Nichols PID Gains for Roll and Pitch Subsystems	42
4.5. Roll Proportional Gain (K_p) Table	45
4.6. Roll Derivative Gain (K_d) Table	45
4.7. Pitch Proportional Gain (K_p) Table	45
4.8. Pitch Derivative Gain (K_d) Table	45
4.9. Pitch Integral Gain (K_i) Table	46

A. Source Code Repositories

This chapter contains references to the public GitHub repositories containing the source code and models developed for this thesis.

A.1. PSM Firmware

Contains the source code for the Power Supply Module (PSM). **Repository URL:**

https://github.com/liamjosephnolan/psm_src

A.2. MTM Firmware

Contains the source code for the Master Thesis Motor (MTM) controller. **Repository**

URL: https://github.com/liamjosephnolan/mtm_src

A.3. MATLAB Scripts

Contains the MATLAB scripts used for system identification, controller design, and generating plots for this thesis. **Repository URL:** <https://github.com/liamjosephnolan/>

thesis_matlab

A.4. MTM SDF Model

Contains the Simulation Description Format (SDF) model of the MTM for use in the Gazebo simulator. **Repository URL:** https://github.com/liamjosephnolan/mtm_sdf

A.5. MTM Joint Publisher

Contains the source code for the ROS 2 node that acts as a bridge between the MTM Micro-ROS node and the Gazebo SDF model. **Repository URL:** https://github.com/liamjosephnolan/mtm_joint_publisher ""